Corrosion of titanium alloys in pressurised water at 300 °C and 350 °C

Sabrina Selva, Quentin Bignon, Quentin Auzoux, Frantz Martin, Amandine Raynal, Frédéric Miserque, Michel Tabarant, Laurence Latu-Romain, Yves Wouters

Version of Record: https://www.sciencedirect.com/science/article/pii/S0010938X21004121
Manuscript_78b88e1b45b5f2ebe62062b611fda14f

Corrosion of titanium alloys in pressurised water at 300 °C: kinetics and modelling.

Sabrina SELVA[1,3], Quentin BIGNON[1,3], Amandine RAYNAL[1], Frantz MARTIN[1], Quentin AUZOUX[1], Gilles RENOU[3], Michel TABARANT[2], Frédéric MISERQUE[1], Laurence LATU-ROMAIN[3,4], Yves WOUTERS[3]

[1] *Université Paris-Saclay, CEA, Service de la Corrosion et du Comportement des Matériaux dans leur Environnement, 91191, Gif-sur-Yvette, France*

[2] *Université Paris-Saclay, CEA, Service d'Etudes Analytiques et de Réactivité des Surfaces 91191, Gif-sur-Yvette, France*

[3]*Université Grenoble Alpes, CNRS, SIMaP, 38402, Saint Martin d'Hères, France*

[4]*Ugitech, Centre de recherches, Av. Paul Girod, 73400 Ugine, France*

ABSTRACT

The corrosion of titanium alloys in primary water at 300 °C led to a global weight gain due to oxidation and surface precipitation, despite some dissolution. A model was proposed, taking into account the weight contribution of each oxide type to the global mass evolution with exposure time. Based on this model, on mass variation and GD-OES results, a corrosion rate ranging between 2 and 6.6 µm.year^{-1} at 300 °C for all tested materials was estimated. Due to the simultaneous corrosion of the used stainless steel reactors, a protective ilmenite layer finally precipitated at the surface of the samples.

KEYWORDS

Titanium, Corrosion, Anatase, Rutile, Ilmenite, Pressurised water

1 Introduction

Titanium alloys could be good candidates for nuclear Pressurised Water Reactor (PWR) primary circuit structure components. They could indeed replace some stainless steel parts because of their lower neutron activation and their good mechanical properties [1]. In this type of environment, the operating temperature is around 300 °C and the water is pressurised at 15 MPa. In order to estimate the durability of the materials under these conditions, where corrosion can be an issue, the present study was conducted in simulated PWR primary water at 300 °C, nominal conditions. The corrosion mechanisms of CP (Commercially Pure) Ti, Ti64 (also called Ti-6Al-4V) and Ti10-2-3 were priory established at 300 °C, 15 MPa at $pH_{25°C}$ = 10.1 by Bignon *et al.* [2], for exposure durations up to 834 h. It was determined that small crystallites of anatase TiO_2 and large micrometre-scale crystallites of ilmenite $FeTiO_3$ formed on the surface of a continuous nanometre-scale oxide layer made

of rutile TiO_2 for CP Ti and of anatase for Ti64 and Ti10-2-3 that covered the exposed materials. These crystallites resulted from the precipitation of titanium and iron hydroxides that originated respectively from the dissolution of the continuous oxide layer and the stainless steel experimental device [2].

These features are in agreement with the very few works dedicated to the study of the corrosion behaviour of titanium alloys in primary water, even if in slightly different conditions such as pressurised water [3] and supercritical water [4]. Zhang *et al.* [3] exposed samples of commercially pure titanium TA1 ELI (O < 0.1%wt) up to 3064 h to pure water at 8.6 MPa, 300 °C and at neutral pH at 300 °C in a stainless steel autoclave. They reported that the oxides formed on the surface of the samples were mainly brookite TiO_2 and Ti_8O_{15} crystallites with a small amount of crystallites containing iron and nickel without without specifying the state of the oxygen detected, *i.e.* O in solution in intermetallic FeNi or in oxide phase. Kaneda *et al.* [4] exposed Ti-3Al-2.5V, Ti-15V-3Al-3Sn-3Cr, and Ti64 during 500 h to pure supercritical water (25 MPa, 290-550 °C, 8 wt.ppm of dissolved oxygen) in a device composed of aluminium parts. The authors observed, as Bignon *et al.* [2], the presence of a continuous oxide layer and particles on the surface of the samples at 290 °C and at 550 °C, but did not study the composition of these oxides at 290 °C.

In literature, most of the corrosion kinetic studies rely on the mass variation measurements in order to estimate the evolution of the corrosion rate over exposure duration. For instance, Kaneda *et al.* measured after 500 h exposure at 290 °C, a weight gain of 12 ± 2 $mg.dm^{-2}$ for Ti-3Al-2.5V and of 10 $mg.dm^{-2}$ for Ti64 [4]. After 500 h spent in boiling pure water at 300 °C and 8.6 MPa, Zhang *et al.* obtained for CP Ti a weight gain of around 2 $mg.dm^{-2}$ [3]. However, as suggested earlier by the complex evolution of the corrosion products on these alloys in pressurised water, the conversion from mass variation to corrosion rate may not be obvious, due to concomitant oxide dissolution - weight loss - and oxidation / precipitation processes - weight gain.

One of the key issues in such studies involving mass variation measurements is to link it with a corrosion rate or oxidation rate, which is the main information needed for service life previsions. Different strategies have been adopted in literature. Zhang *et al.* chose to first fit their data with a parabolic model ($\Delta m/S = at^b$, with b = 0.51) and a power law model ($\Delta m/S = at^b$, with b = 0.67) [3]. This type of approach is widely used for the study of Zr-based alloys in pressurised water environments [5]–[7] since the zirconia layer grown over these alloys in such environment does not dissolve in the media, which makes the conversion of mass gain into corrosion rate quite direct. Thus, this approach might not apply for titanium alloys that undergo both dissolution and reprecipitation at their surface during exposure in similar

media. However, Zhang *et al.* assumed that, despite the presence of crystallites and corrugation on the surface, the oxidation rate limiting step for CP Ti under their conditions was diffusion through the TiO_2 oxide layer, which allowed for a direct equation linking the specific mass uptake and the supposedly uniform oxide thickness [3]. The calculated value was 1.4 times higher than the cross-section oxide thickness measurement albeit carried out on a crystallite. In light of these inconsistencies, and the surface oxide morphologies found by Bignon *et al.* [2], it appears that the extraction of the corrosion rate from gravimetric studies for titanium alloys in primary water is not straightforward and needs further thorough investigations: this point constitutes the main goal of the present paper. This statement is in agreement with Kaneda *et al.* [4], who claimed that corrosion rate estimates based on weighing were unreliable since the measurement took into account mass gain due to precipitation and mass loss due to dissolution of the basic elements. They suggested that it was preferable to make estimates based on continuous oxide thickness measurements. However, Macdonald [8] showed that not all the equations involved in corrosion necessarily resulted in the movements of the boundaries of the continuous oxide layer. These movements caused a change in the thickness of the oxide layer. He classified the reaction in two types: the lattice non-conservative reactions, which induced a change in the thickness of the oxide layer and the lattice conservative reactions, which do not. However, these two types of reactions will both affect the mass variation of the sample. Therefore, there is no consensus on the method to be used for estimating the actual corrosion rate under these conditions.

Another strategy, adopted for stainless steels exposed to PWR, would be to take into account all the equations mentioned by Macdonald in the Point Defect Model approach [8] and only the mass loss due to dissolution of species: the corrosion products are thus dissolved electrochemically under acidic conditions to estimate the consumption of alloy. Using this method, Sekine *et al.* estimated for a 304L stainless steel (SS) a weight loss of 25 $mg.dm^{-2}$ after 200 h of exposure to a PWR medium at 288 °C: the associated corrosion rate was of the order of 21 $\mu m.year^{-1}$ [9]. After 200 h exposure, the corrosion kinetics of stainless steels decreased sharply due to the formation of a protective oxide [10]. It led to a corrosion rate drop down to less than 0.2 $\mu m.year^{-1}$ for SS 309L exposed in autoclave to PWR environment (800 wt.ppm of B as H_3BO_3 and 2.2 wt.ppm of Li as LiOH) at 300 °C, for tests lasting 124 and 399 days [11].

A major disadvantage of this technique is that it requires to check that all the oxide has been effectively dissolved, which can be all the more difficult if the metal/oxide interface is very rough. However, this method cannot be carried out for titanium alloys since TiO_2 is very difficult to dissolve, especially for micrometre-range thicknesses, and cannot be reduced

electrochemically. Be that as it may, the corrosion rate of titanium and its alloys at 300 °C or higher temperature, in PWR primary water conditions has never been estimated to date: it is the objective of the present study. However, it must rely on sufficiently relevant results and observations made on long enough exposure durations to ensure that (i) the collected data are reliable over time and (ii) the formerly evidenced mechanisms at durations up to 834 h exposure are still valid for longer times. This latter point will be the object of a preliminary part consisting in additional analyses of the microstructural evolutions of the oxides system at long exposure times, aiming at verifying the ongoing corrosion mechanisms identified earlier in [2] are still valid up to more than 11 000 h exposure, for all three studied materials, *i.e.* CP Ti, Ti64, Ti-10-2-3.

In a second part, the evolution with time of the different individual steps of the corrosion mechanism involved in mass variation will be studied, for all three materials, and their kinetics evaluated thanks to a series of analyses detailed later on. Based on mass variation measurements and on these corrosion mechanisms, a method for the corrosion rate estimation will be proposed and discussed.

2 Materials and procedures

2.1 Materials

The studied materials belong to different metallurgical families of titanium alloys. The commercially pure titanium, referred to as CP Ti, is a single-phase α. The other studied alloys are Ti64, which is a two-phase α+β alloy with 4 vol.% of β phase and Ti10-2-3, which is a β-metastable alloy with 38 vol.% of β phase. The α/β volumetric phase ratios were determined by Electron BackScattered Diffraction (EBSD). CP Ti belongs to the grade 2, Ti64 is composed of 6 wt.% Al and 4 wt.% V and Ti10-2-3 of 2 wt.% Fe, 3 wt.%. Al and 10 wt. % V. The detailed chemical compositions for the three alloys used in this work are available in [2].

The three billets, supplied by TIMET Savoie in the mill-annealed state, were hot-rolled and treated for two hours at 675 °C, 730 °C and 760 °C for CP Ti, Ti64 and Ti10-2-3, respectively. The resulting microstructures are reported in [2]. The structure of CP Ti is composed of equiaxial grains with an average size of 60 µm while that of Ti64 and Ti10-2-3 is bimodal with a grain size of the order of a few µm. Typical dimensions of the specimens were 20 x 10 x 1 mm^3, sampled by machining parallel to the transverse plane of the billets.

EBSD analyses performed on the specimens [12] indicate that the c-axes of the α hexagonal unit cells of the CP Ti and Ti10-2-3 are preferentially oriented in the transverse direction, which is the sample length. For Ti64, they are predominantly oriented in the rolling direction of the billets, which is the sample thickness. The samples were ground with SiC paper from grit 500 down to grit 2400 then polished with diamond suspensions (down to 1 µm). Finish polishing was carried out with colloidal silica suspension (pH = 9).

2.2 Primary water exposure

PWR primary water was simulated by using pressurised and heated ultrapure water at 15 MPa and 300 °C, containing 0.9 wt.ppm of Li^+ added in the form of LiOH and dissolved hydrogen, specified later. The pH value was set by LiOH and varied with temperature, as the pK_{water} value changes with temperature. In pressurised water at 25 MPa, the pH of a neutral solution was estimated to be 5.56 [13]. The impact of pressure on these values was assumed negligible for pressures ranging between 15 and 25 MPa. The pH was 10.1 at 25 °C, leading to a $pH_{300\ °C}$ = 7.2. To prevent galvanic coupling between titanium alloys specimen and stainless steel of the body of the set-ups, the samples were suspended thanks to oxidized zirconium wires or supports.

Different device configurations were tested, allowing either dynamic fluid conditions or static fluid conditions to be investigated. In dynamic conditions, the water was continuously renewed and purified in a recirculation loop. These conditions were used to be more representative of nuclear reactor primary circuit conditions, although the fluid speed was much lower than in the reactor. Static conditions were used to investigate stagnant water conditions and longer exposure durations, not achievable with the corrosion loop at the laboratory time-scale. These two different experimental set-ups, as well as their specificities are detailed thereafter.

2.2.1 Dynamic environment

The experimental device used to expose the samples to primary water under dynamic conditions was a stainless steel corrosion loop as shown in Figure 1, as typically used in corrosion studies in primary water [14], [15], [16]. The cold part - at room temperature - of the loop is schematised on the left side (blue colour) and the temperature-regulated part (red

colour) is on the right side. The elements positioned between the pump and the pressure regulator such as the expansion valve, were operating at high pressure. The originality of this set-up lies in the presence of two reactors placed one after the other. A valve system was used to bypass the downstream reactor called R2 so that the sample holder can be removed from this reactor without affecting the upstream reactor called R1.

The hydrogen concentration in the water was set by the pure hydrogen gaseous atmosphere of $P(H_2)$ = 1.4 x 10^5 Pa thanks to the Henry's law inside the cold tank, which was continuously monitored and possibly adjusted throughout the experiment. The dissolved hydrogen concentration at high pressure and high temperature was 25 × 10^{-6} $m^3.kg^{-1}$ H_2O NTP (normal temperature and pressure), equivalent to 2.25 wt.ppm of H_2. During the tests, the water flow was set at 5.10^{-3} $m^3.h^{-1}$ leading to a water velocity of 4.7 $m.h^{-1}$ at the samples' surface. After being pressurised, the primary water was heated up to 300 °C in the pre-heater. The heating and cooling rates of the temperature transients were + 300 °C.h^{-1} and – 60 °C.h^{-1}, respectively. The temperature difference between the top and the bottom of each vertical reactor was below 4 °C during thermal transients and inferior to 1 °C under isothermal conditions. After passing in the reactors, the media was cooled down then depressurised before being purified by the ion-exchange resins, which captured a part of the cations (corrosion products) dissolved in the water. In order to prevent any variation in lithium concentration at that stage, the ion exchange resins were saturated at $[Li^+]$ = 0.9 wt.ppm with lithium hydroxide before any test. Due to the position of the ion exchange resins in the corrosion loop, the primary water feeding the upstream reactor (R1) was well purified. However, corrosion products generated in R1 may contaminate the media that enters the downstream reactor (R2).

Test durations were 24 h, 89 h, 217 h, 434 h, 834 h, 1632 h and 3499 h. An important point to notice is that the short duration tests were conducted in the downstream reactor (R2) whereas the long duration test (3499 h) was carried out in the upstream reactor (R1).

Once removed for examination, the samples were not re-exposed to the media: fresh specimens were thus introduced for each tested exposure duration. In order to increase statistical representativeness, for each condition and time, three samples per alloy type were immersed.

2.2.2 Static environment

The set used here consisted in an autoclave, wherein the specimens were immersed. A gaseous sky was composed of a mixture of argon and 1 % molar hydrogen gas at 2.45 MPa at 300 °C. It was in contact with the liquid medium and fixed the hydrogen content in the water to ensure a dissolved hydrogen concentration of 25 × 10^{-6} $m^3.kg^{-1}$ H_2O (NPT). In addition, the vapour-liquid equilibrium established at 300 °C gave rise to a pressure of 8.58 MPa, which means the total pressure in the autoclave at 300 °C for these tests was fixed at 11 MPa. The heating and cooling rates applied during temperature transients were + 30 $°C.h^{-1}$ and - 18 $°C.h^{-1}$ respectively. The temperature difference between the top and bottom of the autoclave was less than 3 °C at 300 °C.

Exposure durations were 3505 h (5 months), 7560 h (10 months) and 11065 h (15 months). Samples were exposed for 3505 h and 7560 h in the autoclave, with no re-exposure during these durations. For practical reasons, some of the 7560 h autoclave samples were then re-exposed for 3505 h to make up the 11065 h exposure.

2.3 Characterisation techniques

The weight of each sample was measured before and after exposure to primary water on a XPE26/A Mettler Toledo balance, which has an accuracy of 10^{-6} g. X-ray diffractograms on the sample surfaces after exposure to media were acquired thanks to a PANalytical X'Pert PRO MPD X-Ray Diffractometer (XRD): the analysed surface, at grazing incidence (1.5 °), was 7 × 7 mm^2. The sample surfaces were observed with an Ultra 55 Zeiss Field Emission Gun Scanning Electron Microscopy (FEG-SEM) at 5 kV. Polished cross-sections of the samples were also observed with this FEG-SEM, once their surfaces were protected by Au sputtering and Ni electroplating. The FEG-SEM was equipped with a XFlash Detector 4010 Bruker Energy Dispersive Xray Spectrometer (EDS), which was used with an incident electron beam accelerated at 20 kV. The identification of the nature of microscopic oxides was performed by a Horiba XploRA™PLUS Raman spectrometer with a laser wavelength of 532 nm. The analysed surface was 1 μm^2 and the analysed depth was 1 to 2 µm.

The elementary concentration profiles in function of the analysed depth for the three materials before and after exposure were obtained by using (i) a Profiler 2 Horiba Scientific Glow Discharge – Optical Emission Spectroscopy (GD-OES) (with P = 25 W and P(Ar) = 8.5 mbar no-pulsed mode) and (ii) a Thermofisher Escalab 250 xi X-ray Photoelectron Spectrometer (XPS). The XPS used an Al Kα X-ray source (1486.6 eV) and was equipped with an Ar^+ ion sputtering gun. The analysed surface by XPS was around 0.6 mm^2 with an analysed depth of around 10 nm. For GD-OES, the analysed surface was 12.5 mm^2. 50-nm-

thick foils of the transversal cross sections were previously prepared with a dual-focused ion beam scanning electron microscope (FIB-SEM, Zeiss Cross Beam 750 for the foil extraction and a FEI Strata DB400 for its thinning), then observed with a TEM (FEI Tecnai Osiris). Nanoscopic oxide phase maps were acquired by using the precession-assisted crystal orientation mapping technique, ASTAR, which is a TEM-based diffraction spot recognition technique [17] realised on a FEG-TEM Jeol 2100F at 200 keV. This TEM was also used in STEM mode with 1 nm spot size. The software ImageJ™ was used for post-treatment and image analyses.

3 Results

3.1 Characterisation of the oxides formed after long exposure duration

In order to check that the corrosion mechanism proposed in [2] was also valid for the long exposure durations, additional analyses were carried out on the samples exposed for 3499 h, the longest time to the dynamic medium. Moreover, observations were also made on the samples exposed up to 11065 h to the static medium in autoclave.

CP Ti sample exposed during 3499 h at 300 °C to primary water was analysed by XRD at grazing incidence (1.5 °, detection limit of 1 vol.% of an element). The analysed depth was of few micrometres. Figure 2 shows the associated XRD diffractrograms and the phase indexation with the references from the International Centre for Diffraction Data (ICDD). The Ti-α phase of the metal was detected (Ref: 00-044-1294), which means that the entire thickness of the oxide layers was analysed. The oxides formed on the surface were identified as anatase TiO_2 with tetragonal structure (Ref: 00-021-1272) and ilmenite $FeTiO_3$ with trigonal structure (Ref: 04-007-2813). Rutile TiO_2 with tetragonal structure (Ref: 00-021-1276) was also detected at $2\theta = 27.5$ °, $d_{110} = 0.325$ nm. All these results are in agreement with the XRD analyses at 434 h exposure in the same environmental conditions shown in [2].

Cross-section observations of samples of the three materials exposed for 217 h, 834 h and 3499 h at 300 °C in primary water were also carried out by SEM with secondary electrons. Figure 3 shows the evolution with exposure duration of the CP Ti surface observed in cross-section. The large $FeTiO_3$ crystallites were easily observable and some small crystallites in TiO_2 were also visible. As for specimen exposed for a shorter time presented in [2], the identification of the nature of the large and small crystallites was carried out by µ-Raman spectroscopy (not shown here). Beneath these crystallites, a very thin continuous oxide layer was always present.

The presence of holes shown in Figure 3.c and d) can be assigned to zones where the metal consumption was strongly in progress, but their surface is still covered by a thin continuous oxide layer (see Figure 3.d). It seems that beneath the $FeTiO_3$ crystallites, no or much less metal consumption occurred, as suggested by the flat interface. These local variations of metal consumption led to an increase in the tortuosity of the metal/oxide interface with the exposure duration (see Figure 3). This morphology was also observed for Ti64 and Ti10-2-3 at all exposure durations. The nature and morphology of the oxide after 3499 h exposure of CP Ti, Ti64 and Ti10-2-3 are consistent with the mechanism presented in [2].

However, it should be noted that after 3499 h exposure, the oxide layer grown on CP Ti only became remarkably spongy in the local attack sites with a depth of more than 400 to 500 nm, as illustrated by the traces of oxides pointed with black arrows in Figure 3.c) and d). For shorter exposure duration, even 1632 h, the depth of the local attack sites remained below around 200 nm and this spongy aspect was not noticed. For Ti64 and Ti10-2-3, this spongy layer was always negligible. This particularity was not observed before 3499 h in the study of Bignon *et al.* [2]. As discussed in this cited work and only for CP Ti, the nature of the oxide could inform us about their formation mechanism. Indeed, anatase would mean that these traces come from precipitation at the medium/oxide interface whereas rutile means that they come from the metal oxidation at the metal/oxide interface. Due to the size of the particles of interest, the nature of the spongy oxide layer was characterised by TEM-ASTAR from a TEM thin foil extracted from CP Ti exposed 3499 h at 300 °C. Figure 4.b) illustrates that rutile was detected in the spongy zone (yellow square). It can be inferred that the spongy oxide layer is composed of rutile nanograins with no preferential orientation as it is shown in Figure 4.c).

The STEM-EDX mapping and concentration profiles of titanium and oxygen performed on this TEM foil are presented in Figure 5. The profiles made along 2.3 µm depth and integrated on a 500 nm large band (shown in blue) indicate a sharp increase of the oxygen concentration near the protective deposit/oxide interface and a clear decrease at the oxide/metal interface with a resolution of a few nanometres. The measured intensity of oxygen signal in the substrate was below the sensitivity limit of EDS, no “O signal” gradient was detected in the metal from the oxide/metal interface. The titanium concentration, for its part, increased with depth and was highest in the substrate. Note that this increase of Ti signal in the bulk metal was simply due to the increase in thickness of the thin foil. It was also evidenced in the bright field image with the decrease in the transparency toward the bottom of the image.

No local attack sites was observed on the cross-sections of the samples exposed in the autoclave, regardless of the material and the exposure duration. On the specimens exposed

for 7560 h at 300 °C in the autoclave, duration which is twice larger than the one investigated in the loop, the surface was fully covered by ilmenite crystallites whatever the investigated titanium alloy, as illustrated in Figure 6. This full coverage was also observed at 11065 h exposure and was almost reached at 3505 h exposure. As for the exposure in dynamic medium, a nanometric TiO_2 layer with a constant thickness of around 30 nm was always present under the ilmenite crystallites. However, very few TiO_2 crystallites were detected.

3.2 Corrosion kinetics during exposure to primary water

As mentioned in the introduction and as shown in [2], the three tested alloys undergo dissolution and some re-precipitation during their exposure to primary water. These different mechanisms occurring at the same time in unknown proportions, it prevents any classical corrosion kinetics study based on simple mass evolution measurements. Keeping in mind the objective to determine accurately the corrosion rate from mass variation measurements, the individual contributions of each phenomenon, *i.e.* dissolution, evolution of the oxide/metal interface and precipitation, have first to be studied and evaluated separately. Intensive characterisations of the evolution of all surface/interface oxide features with exposure duration are the object of the present section.

3.2.1 Continuous oxide layer and interface tortuosity

The initial thickness of the native continuous oxide due to the natural exposure to air, was determined by XPS, which has a detection limit in depth analysis of around 6 nm. This limit is considered to be three times the inelastic mean free path estimated at 2.16 nm for TiO_2 [18]. By comparing the relative intensities of signals associated with electrons coming from a metal and an oxide environment (*e.g.* on Ti 2p binding energy spectra), the thickness of the native continuous oxide layer was estimated at 4 nm for CP Ti and Ti64 and at 3 nm for Ti10-2-3. As the metallic substrate was detected during analyses, it can be reported that, taking into account the uncertainties, the thickness of the native continuous oxide layer for all materials was below 6 nm.

For each exposure duration in corrosion loop, the continuous oxide layer thickness was measured on cross-sections by SEM in secondary electrons, averaged over 20 images taken at different areas on the specimens. Figure 7 gathers the associated results for the three exposed materials. The establishment of a steady state in the continuous oxide layer thickness is highlighted, reaching for CP Ti an average continuous oxide thickness of 30 nm. The initial transient was rapid. The average steady-state thickness of the continuous oxide

layers on Ti64 and Ti10-2-3 appeared to be slightly less than that of CP Ti, reaching 23 nm for both materials. The measurements carried out on specimens coming from the two different reactors R1 (upstream) and R2 (downstream) are in good agreement with each other, showing no specific effect of the position in the circuit on this continuous oxide layer thickness.

The evolution of the interface corrugation along with exposure duration indicates local accelerated corrosion of the metal. This geometrical aspect was used to estimate the amount of corroded metal with exposure duration, provided the initial surface of the sample was known. Assumption was made that ilmenite deposition on the surface occurred in the early stages of the exposure; the interface between ilmenite crystallites and the metal - with a thin TiO_2 layer in-between - was relatively flat, which may support this hypothesis. Hence, the method presented in Figure 8 consisted here to estimate by SEM cross-section image analysis the mean corroded metal depth by tracing the initial interface along the bottom of all ilmenite crystallites. Then the corroded metal areas, hatched in red in Figure 8 was selected, and finally divided by the length of the image.

This image analysis procedure was performed on 20 SEM images for each exposure duration and material for statistical purpose. Note that using this method probably underestimates the mean depth of corroded metal due to the uncertainties on the placement of the reference line: the actual position of the initial surface was probably not the one used here, which could have shifted towards the metal in the first steps of exposure before being covered by ilmenite.

Figure 9 shows the as-estimated mean depth of corroded metal evolution with exposure duration for all three alloys at 300 °C. The kinetics of the mean corroded metal depth evolution was approximately linear for all three materials regardless of the reactor of exposure.

An additional information extracted from these image analyses is that the ratio of the maximum corroded metal depth in the local attack sites to the mean corroded metal depth was constant (between 3 and 4) for each exposure duration and material. It means that the local attack sites identified around the $FeTiO_3$ crystallites were not pits. The linear evolution with exposure duration of the mean corroded metal depth, for all materials, indicated that, after a short transient, the corrosion rate was constant with the exposure duration in both reactors and independent of the reactor. Despite the uncertainty in the placement of the reference line to estimate the volume of metal actually corroded, these measures allowed the estimation of a lower bound of the corrosion rate. It was, according to Figure 9, on average

the same for all three materials. The minimum corrosion rate would thus be around 0.9 µm.year^{-1} at 300 °C in the dynamic medium.

As shown in Figure 6 after exposure of the materials in the autoclave at 300 °C, the metal/oxide interface was very tortuous between the $FeTiO_3$ crystallites and relatively flat below them. This aspect allowed the same approach as mentioned above to be applied to the samples exposed in the autoclave from 3505 h to 11065 h at 300 °C. Under static conditions, the average corroded metal depth was estimate about 0.4 µm for all materials, whatever the investigated exposure duration above 3505 h, suggesting a very low corrosion rate beyond 3505 h. It is noteworthy that the corroded metal depth reached after 3505 h in the autoclave was almost identical to the one reached after 3499 h in the corrosion loop. The minimum corrosion rate would then be around 1 µm.year^{-1} since 0.4 µm of metal were corroded in 3505 h corresponding to 0.4 year at 300 °C before complete coverage by ilmenite in the static medium.

3.2.2 Crystallites precipitation

Microscopic observations showed that there were numerous $FeTiO_3$ crystallites on the surface of the samples and that they seemed to protect locally the nanometric oxide layer from corrosion. Two aspects of these surface crystallites will be developed in this part: first, the proportion of ilmenite on the overall oxides over time will be estimated, and second, focus will be made on the evolution of the ilmenite coverage ratio with increasing exposure duration.

As the oxide layer is mainly made of $FeTiO_3$ ilmenite and TiO_2 anatase crystallites, plus the nanoscale TiO_2 oxide layer – rutile or anatase, depending on the material –, and assuming that the titanium only comes directly from the dissolution of the metal/alloy, the iron and oxygen atoms in these oxides contribute to the mass uptake of the samples. GD-OES technique has been used to perform concentration depth profiles on the samples, from the surface, after their exposure to the media. This technique permits to quantify elements – here Ti - O - Fe – on an area of 13 mm² and on 10 µm in depth. The measures were assumed representative of the whole surface of the specimens. The boundaries of these integrals range from 0 to 1.2 µm, depth beyond which [O] < 10 %, value that was taken to mark the oxide/metal interface in Figure 10. These integrals give the area under the curve called A_O for oxygen and A_{Fe} for iron in Figure 10 for the Ti10-2-3 sample exposed 834 h at 300 °C. This value was taken arbitrary and seems to be a good compromise not to overestimate the oxygen amount. Indeed, if the signal is integrated over all the analysed depth, the background noise of the oxygen in the GD-OES, estimated around 1 – 4 at.%, would also be

taken into account and lead to overestimations. Note that the dissolution of O in Ti is neglected which is relevant according to the STEM-EDX characterisations, shown in Figure 5 carried out on samples exposed 3499 h at 300 °C. Taking advantage of the fact that the stoichiometric coefficient of the iron in $FeTiO_3$ ilmenite is one, the integration of the Fe concentration profile gives the Fe amount n_{Fe}, which documents the ilmenite amount n_{FeTiO3}, while the oxygen amount n_O documents both oxides types. Note that Ti signal cannot be used since it also belongs to the metallic matrix. According to the stoichiometry of each oxide, the amounts of ilmenite n_{FeTiO3} and of anatase n_{TiO2} can be evaluated by Eq.1 and Eq. 2:

$$n_{FeTiO3} = n_{Fe} \quad \text{(Eq.1)}$$

$$n_{TiO2} = \frac{n_O - 3n_{Fe}}{2} \quad \text{(Eq.2)}$$

From these amounts of substance, it was possible to calculate q, the ratio of the amount of titanium that participates to $FeTiO_3$ ilmenite crystallite edification, namely n_{FeTiO3}, over the total amount of titanium participating to the total oxide edification, namely $n_{FeTiO3} + n_{TiO2}$, written as (Eq. 3):

$$q = \frac{n_{FeTiO3}}{n_{FeTiO3} + n_{TiO2}} \quad \text{(Eq.3)}$$

Figure 11, gathering the values of the evolution of the ilmenite fraction q as function of exposure duration, at 300 °C for the three materials tested, shows an approximately linear increase in the ilmenite fraction with exposure duration independently of the reactor (upstream R1 or downstream R2). For all exposure durations, the ilmenite fraction was always lower for Ti64 compared to other materials. The slopes α of each linear fit are reported in Table 1.

In addition, as ilmenite crystallites grow over time and as corrosion beneath them seems very slow, as shown in Figure 3, the surface coverage ratio by $FeTiO_3$ crystallites might be an important parameter to focus on. Image analyses of surface optical microscope observations have therefore been carried out to follow its evolution with exposure duration at 300 °C. Ilmenite crystallites were easily spotted thanks to their size and shape distribution. For each exposure duration and material, 10 images were analysed, which represented a minimum surface area of 200 mm² depending on the magnification, which was assumed representative of the material's surface. Figure 12 illustrates the increasing evolution of the $FeTiO_3$ crystallites surface coverage ratio as a function of exposure duration for all materials.

Obviously, the coverage of the surface by ilmenite crystallites increases with exposure duration, whatever the material. Nevertheless, the coverage ratio for samples exposed in the loop, in both reactors (Figure 12) remained well below 1. Linear trend curves, for samples exposed in the downstream reactor 2 only, have been plotted in Figure 12. The coverage ratio seems to increase linearly with exposure duration. Note that initial coverage ratio should be zero and that coverage kinetics might not have been linear in the first moments.

A rough extrapolation of the in-loop coverage for exposure durations of around 8000 h, according to data presented in Figure 12, would lead to coverage ratios around 0.3 to 0.5. The full coverage observed in autoclave (see Figure 6) after 7560 h exposure was attributed to the fact that the media in the autoclave was not renewed due to the absence of ion exchange resins, allowing a quicker saturation of water by Fe and Ti ions.

3.2.3 Mass variation

The mean specific mass variation of the samples of the three materials for each exposure duration at 300 °C are shown in Figure 13. A positive mass uptake was measured for all three materials for any exposure duration. The mass uptake kinetics of CP Ti and Ti10-2-3 were slightly higher than the one of Ti64. As suggested in Figure 13, the mass uptake in the upstream reactor, albeit positive, was slightly lower than the one in the downstream reactor: focusing on reactor 2 data (downstream), the weight gain kinetics was approximately linear for all three materials. The mass uptake of samples exposed in the upstream reactor (R1) (3499 h at 300 °C), especially for CP Ti and Ti10-2-3, were lower than expected by following the trend of the samples exposed in the downstream reactor (R2).

These weight gain measurements were compared in Figure 14 to data obtained in the static configuration, which is an autoclave without recirculation loop nor ion exchange resins. The mass gain of the three materials in the autoclave was greater than that of the samples exposed for 3499 h in reactor 1 of the loop at 300 °C. The long exposure durations in autoclave also showed a stabilisation of the weight gain after 7560 hours of exposure for all three materials. In autoclave, the mass gain of CP Ti appeared to be slightly higher than that of Ti64 and Ti10-2-3.

According to each kinetics study mentioned in this section, the growth of the continuous TiO_2 oxide layer and the TiO_2 and $FeTiO_3$ crystallites precipitation on the samples' surface imply a global mass uptake. However, the metal dissolution estimated by the corroded metal depth kinetics contributes to a mass loss. Thus, these mass uptake evolutions with exposure duration are difficult to interpret directly, since they are the convolution of all these

phenomena. This point will be discussed in the following section in order to propose a method for the estimation of the corrosion rate.

4 Discussion

4.1 Corrosion mechanisms at 300 °C

Figure 15 schematically summarises the global corrosion mechanisms at 300 °C, according to [2], showing these dissolution / precipitation-coprecipitation mechanisms. As for the origin of iron in $FeTiO_3$ ilmenite, it was supposed that it was brought by the medium in the form of iron hydroxides, coming from the corrosion and partial dissolution of the experimental device made of 316 L stainless steel. The possibility of TiO_2 dissolution was in agreement with the significant value of the TiO_2 solubility in water which is around 1.2×10^{-8} mol. kg^{-1} H_2O and with the steadiness of the continuous oxide layer after around 200 h exposure at 300 °C as shown in Figure 7 and discussed later (see. 3.2.1) [19]. At the $pH_{300\ °C}$ = 7.2 of the present study, dissolution of TiO_2 in water led to the formation of $Ti(OH)_4$ and $Ti(OH)_5^-$ hydroxides [20], illustrated by the step 1 in Figure 15. Some of these Ti-containing aqueous species can either precipitate to form the crystallites, or be taken away from the specimen by the medium, especially in the case of the loop (see step 2 in Figure 15). Once locally the solubility limit was reached, precipitation under the form of TiO_2 anatase or coprecipitation in $FeTiO_3$ ilmenite could take place (step 3 in Figure 15). Reaching the solubility limit at the interface between the medium and the continuous oxide layer depends on several factors, such as local pH, natural convection, media speed, etc. Then, the crystallites grow up as shown in the step 4 in Figure 15 until the total coverage of the surface.

Dissolution of the continuous TiO_2 oxide layer does not seem to occur much beneath the $FeTiO_3$ crystallites, which makes the kinetics of $FeTiO_3$ coverage ratio particularly important to estimate. This feature created protected zones, located beneath these crystallites, which could act as cathodic sites while some local areas undergo increased metal consumption, creating holes (local anodic sites). Thus, this led to a metal/oxide interface, which becomes more tortuous when the exposure duration increases for all studied materials.

When the holes induced by severe tortuosity reach a depth greater than about 400 nm at 300 °C, it seems that the dissolution of the nanometric oxide layer becomes heterogeneous in these zones, leading to the formation of a spongy oxide layer. Indeed, focusing on CP Ti specimens, a rutile spongy oxide layer was detected according to SEM and TEM-ASTAR

observations in the local attack sites for durations expanding from 3499 h exposure at 300 °C (Figures 3 and 4).

4.2 Towards an estimation of the corrosion rate from mass variation measurements at 300 °C

The present section aims at establishing the relation between the mass variation and the corrosion rate at 300 °C following the proposed mechanism. The simultaneous dissolution and growth of the continuous oxide layer and the resulting evolution of its thickness will first be modelled, then, the precipitation of crystallites - TiO_2 anatase and $FeTiO_3$ ilmenite - on the surface of the sample will be considered in the mass balance.

4.2.1 Modelling the growth kinetics of the continuous oxide layer

Figure 7 shows the establishment of a constant continuous oxide thickness after a short transient for each material while the tortuosity of the metal/oxide interface increased during exposure as shown in Figure 3. This indicated the presence of a mixed corrosion regime, *i.e.* continuous oxide layer growth and simultaneous dissolution.

The evolution with exposure duration of this oxide thickness was consistent with a Loriers-Haycock type model (Eq. 4) [21][22], as shown for CP Ti exposed at 300 °C in Figure 7 by the red lines. The model and experimental data agreed for Ti64 and Ti10-2-3 as well.

$$\frac{db}{dt} = \frac{k_g}{b} - k_d \qquad \text{(Eq. 4)}$$

where b is the continuous oxide layer thickness in nm, t exposure duration in h, k_g and k_d are the growth and dissolution rate constants respectively. Note that this equation is valid away from $FeTiO_3$ crystallites.

During the transient regime, the continuous oxide layer thickness increased due to the predominance of the growth term over the dissolution one. The oxygen involved in the titanium oxidation, which allows the growth of the continuous oxide layer, contributes to the mass uptake. Approaching a limit thickness, $b_{lim} = k_g / k_d$, these two terms balance each other, leading to a steady state regime, as shown in Figure 7. b_{lim} was evaluated to 30 nm at 300 °C for CP Ti. For Ti64 and Ti10-2-3, b_{lim} is worth 23 nm at 300 °C for both materials. As a consequence, the mass uptake due to this layer for each material, is determined by the

growth of its thickness during the transient regime and becomes constant for all the exposures as soon as the steady state is reached.

4.2.2 Modelling the mass variation

As Kaneda *et al.* suggested [4], the estimation of a corrosion rate based only on the mass uptake is not straight-forward in the case of an aqueous environment because of the dissolution and re-precipitation phenomena. Nevertheless, studying separately each step of the mechanism provided information on the corrosion rate.

Specific mass variation ∆m/S for each sample was equal to the sum of the individual contributions described in 4.1.

Firstly, the specific mass uptake $\Delta m(O)_{c\text{-}TiO2}/S$ due to the oxygen involved during the growth of the nanometric continuous oxide layer (referred in Eq. 5 as c-TiO_2 subscript) can be estimated by:

$$\frac{\Delta m(O)_{c-TiO_2}}{S} = \Delta w(t) \frac{\rho_{TiO_2}}{M_{TiO_2}} M_{O_2} \qquad \text{(Eq. 5)}$$

where $\Delta w(t)$ is the difference in continuous oxide layer thickness, measured before and after exposure, M_X the molar mass of element X, and ρ_X the volumic mass of element X.

Then, the corrosion rate of the metal determines the amount of titanium available in solution near the samples before either evacuation into the medium or precipitation on the surface of the samples. The precipitation of titanium hydroxides into TiO_2 crystallites on the surface of the samples leads to a mass uptake due to the incorporation of 2 O. The corresponding amount of substance is the product of the titanium precipitation ratio *p* by the amount of corroded metal. The co-precipitation into $FeTiO_3$ crystallites leads also to a mass gain due to the incorporation of additional Fe and O (compared to TiO_2 vs. Ti stoichiometry), which is proportional to both *p* and *q*, the quotient of the amount of $FeTiO_3$ by the total amount of crystallites precipitated at the surface.

Thus, the mass uptake ∆m(Fe-O)/S due to the precipitation into crystallites at the surface of the samples can be considered as:

$$\frac{\Delta m(Fe-O)}{S} = \boldsymbol{r}\ t\ \frac{\rho_{Ti}}{M_{Ti}} \left[\boldsymbol{p}\ (M_{O_2} + q\ M_{FeO})\right] \qquad \text{(Eq. 6)}$$

where, *r* is the corrosion rate (unknown), *t* the exposure duration (measured), *p* the Ti precipitation ratio (unknown) and *q* the $FeTiO_3$ precipitation ratio (measured). Note that unknown parameters are set in bold font.

Finally, the mass loss Δm(Ti)/S due to titanium dissolution in the medium without precipitation at the surface of the samples is:

$$\frac{\Delta m(Ti)}{S} = -\boldsymbol{r}\, t\, \frac{\rho_{Ti}}{M_{Ti}}[(1-\boldsymbol{p})\, M_{Ti}] \qquad \text{(Eq. 7)}$$

Thus, the sum of all the contributions led to equation 8.

$$\frac{\Delta m}{S} = \frac{\Delta m(O)}{S} + \frac{\Delta m(Fe-O)}{S} + \frac{\Delta m(Ti)}{S} \qquad \text{(Eq. 8)}$$

$$\frac{\Delta m}{S} = \Delta w(t)\frac{\rho_{TiO_2}}{M_{TiO_2}} M_{O_2} + \boldsymbol{r}\, t\, \rho_{Ti}\left[\boldsymbol{p}\frac{M_{TiO_2} + q\, M_{FeO}}{M_{Ti}} - 1\right] \qquad \text{(Eq. 9)}$$

By definition, the ilmenite precipitation ratio *q* stands between 0 and 1. As observed in Figure 11, *q* follows a linear increase with exposure duration and can therefore be expressed as $q(t) = \alpha t$ with *α* values reported in Table 1.

For exposure duration for which $q < 1$, Eq. 9 becomes Eq. 10.

$$\frac{\Delta m}{S} = \Delta w(t)\frac{\rho_{TiO_2}}{M_{TiO_2}} M_{O_2} + \boldsymbol{r}\rho_{Ti}\left[t\ \left(\boldsymbol{p}\ \frac{M_{TiO_2}}{M_{Ti}} - 1\right) + \ t^2\left[\boldsymbol{p}\frac{\alpha\, M_{FeO}}{M_{Ti}}\right]\right] \qquad \text{(Eq. 10)}$$

Under the experimental conditions investigated in the present study and based on the results obtained, both corrosion rate and precipitation ratio were assumed to remain constant over time. It comes from Eq. 9 that the mass variation will follow an order 2 polynomial law with exposure duration *t*. From this expression, mass variation can be positive or negative, depending on the value of *p*, as will be discussed later on.

For greater exposure durations, *q* should saturate at 1, and Eq. 9 would become equation 11:

$$\frac{\Delta m}{S} = \Delta w(t)\frac{\rho_{TiO_2}}{M_{TiO_2}} M_{O_2} + \boldsymbol{r}\, t\, \rho_{Ti}\left[\boldsymbol{p}\frac{M_{TiO_2} + M_{FeO}}{M_{Ti}} - 1\right] \qquad \text{(Eq. 11)}$$

Thus, after 9 000 h to 27 000 h at 300 °C depending on the materials (according to Figure 11 and Table 1), the mass variation would tend towards a linear law. However, it is only true if the corrosion rate and the precipitation ratio are not affected by the total coverage of the surface by $FeTiO_3$ crystallites.

4.2.3 Effect of the position of the samples on the unknown model parameters

Some slight influence of the position of the specimens in the loop, *i.e.* in upstream R1 or in downstream R2 reactor, was observed on the kinetics of ilmenite surface coverage ratio and on the mass uptake kinetics, the latter depending on the former. These differences could originate from the fact that the media circulating in R2 is enriched in cations or soluble iron and titanium species, promoted by corrosion mechanisms occurring in R1. The media arriving in contact with the specimens in R1 was considered of constant composition, since it was purified by the ion exchange resins. The other parameters (b_{lim}, q) were unaffected by the position in the loop despite the difference in chemistry of the media between R1 and R2.

This argument is supported by the observations made in the autoclave, where the media is not renewed and not purified: as shown in Figure 14, the mass variation after 3505 hours in the autoclave is much higher than in R1, whereas the corroded metal depth is identical. It is consistent with reaching more quickly the saturation, without affecting the corrosion rate, thus a higher precipitation ratio p in R2 and in the autoclave than in R1.

For this reason, it was chosen to integrate into the model a dependence of the titanium precipitation ratio p on the reactor from which the samples originate, referred to thereafter as p(R1) and p(R2) for R1 and R2 respectively.

4.3 Estimation of the corrosion rate and the Ti precipitation ratio

The method followed here consisted in adjusting the unknown parameters, *i.e.* the corrosion rate r and the titanium precipitation ratio p, to fit Eq. 10 with experimental data presented in Figure 13. The other parameters detailed earlier associated with each material like q were injected in the equation. Following subsections are dedicated to the indexation of these parameters at 300 °C.

The experimental data treatment of the continuous oxide layer thickness growth using Loriers-Haycock's model leads to the conclusion that the transient was very rapid before reaching a steady state, therefore a steady thickness, in the few ten nanometres range. Considering the size of the anatase and ilmenite crystallites deposited on the surface, of the order of the micron scale, the continuous oxide thickness contribution to the global mass variation of the specimens was assumed negligible for exposure durations longer than 200 hours.

In addition, as shown in Figure 13, the specific mass variation was positive throughout the test durations. As *r*, ρ_{Ti} and *t* are also positive, simplifying Eq. 9 lead to following condition:

$$p > \frac{M_{Ti}}{M_{TiO_2} + q\, M_{FeO}} \qquad \text{(Eq. 12)}$$

Since $q \in [0\,;1]$ and $\frac{\Delta m}{S} > 0$ even at short exposure durations, *p* value has to be at least 0.6 in reactor 2 to fulfil the condition of a positive mass variation whatever the exposure duration. With only one long exposure duration in reactor 1 it was impossible to state on the sign of the mass variation for shorter exposure duration. So $p(\mathrm{R2}) \in [0.6\,;1]$.

Observations made on the reactor effect, due to position in the streamline compared to the ion exchange resins lead to the conclusion that the Ti precipitation ratio in reactor 2 (downstream) was higher than in reactor 1 (upstream), giving another condition: *p(*R2*)* > *p(*R1*).*

The fitting procedure was as follows: first, focus was made on data obtained in R2, with which *r* was determined by fitting using different values of *p(*R2*)* in the [0.6; 1] range. As seen before, the corrosion rate *r* is not affected by the reactor and was independent of the material, so it could be injected in the adjustment of the data points obtained in R1, whose fit gives *p(*R1*) – note that only one data point per material was recorded in R1, inducing a relatively low confidence in the associated fit*. Table 2 gathers some different triplets of values for {*p(*R2*); r; p(*R1*)*} that fit well the experimental data in both reactors, according to Eq. 9. With *p*(R2) = 0.6, the model curve did not respect the approximatively linear behaviour of the mass uptake kinetics before 1632 h exposure, such a low value of *p* was therefore discarded. Note that the difference of mass variation observed between CP Ti or Ti10-2-3 and Ti64 was mainly due to the difference in *q*, which was halved for Ti64 compared to the two other alloys – see Figure 11. Figure 16 shows a typical adjustment of experimental data obtained in both reactors of the loop with *p(*R2*)* = 1, leading to *r* = 2 µm.year^{-1} and *p(*R1*)* ≈ 0.8 and verifying the *p(*R1*)* < *p(*R2*)* condition mentioned above.

In addition, when the samples in reactor 2 of the loop and couples of the Table 2 such as *p*(R2) ≥ 0.8 are considered, the model also fits well the positive mass uptake obtained after 3505 h of autoclave exposure for each material (not shown). This seems to indicate that the precipitation ratio could be the same for samples exposed in reactor 2 of the loop as for those exposed in the autoclave and was greater than 0.8, confirming a higher precipitation ratio in the autoclave and in reactor 2 compared to reactor 1.

The minimum corrosion rate adjusted by using the model, using mass variation measurements, is 2 µm.year^{-1} at 300 °C (see Table 2). The lower limit of the corrosion rate of 0.9 µm.year^{-1} estimated from experiments an image analyses at 300 °C for all materials is in

good agreement with this value. This method of estimating the corrosion rate can be sensitive to the mixed phenomena of dissolution and precipitation. It could give a good approximation of the corrosion rate at 300 °C by relying on global measurements. In view of the corrosion rates of stainless steels in PWR environments obtained for short exposure durations and mentioned in the introduction, titanium alloys seem to be a good substitute for these materials in industrial applications. However, the results obtained in the present study after intermediate exposure durations in the corrosion loop indicated that the titanium dioxide layer did not seem to constitute an as protective oxide layer as it is the case for stainless steels after only 200 hours of exposure. Fortunately, according to ilmenite surface coverage data obtained in loop, and more specifically achieved in autoclave, it would seem that full coverage by ilmenite might play a role as protective layer for long term exposure durations. This point is discussed in the following section.

4.4 Effect of ilmenite coverage on the corrosion rate and consequences on long term extrapolations

The microscopic observations in Figure 3 of the samples exposed in the loop showed that locally, the metal underneath the $FeTiO_3$ crystallites was less consumed than around these crystallites, which led to a very tortuous metal/oxide interface. Due to this particularity, the depth of corroded metal could be measured locally as a function of the exposure duration. Its linear evolution made it possible to deduce that the corrosion rate was constant despite the increase in the ilmenite covering of the surface at 300 °C. Thus, a maximum coverage ratio of 0.25 did not result in a decrease in the corrosion rate.

On the other hand, the autoclave tests in a stagnant environment, which lasted up to 3 times longer than in a loop, showed a drop of corrosion rate by stabilisation of both the depth of corroded metal and the mass uptake after 7560 h of exposure at 300 °C for the three materials (Figure 14). In parallel with this important result, Figure 6 shows that at this exposure duration all three materials were completely covered by ilmenite. This has been confirmed by image analyses with the optical microscope of the surface of the samples exposed for 7560 h and 11065 h in the autoclave at 300 °C. The measurement of the depth corroded metal on samples exposed in autoclave at 3505 h, *i.e.* before complete coverage and in corrosion loop at 3499 h with a coverage ratio of 0.25 showed that the same minimal corrosion rate of 0.9 – 1 µm.year^{-1} was estimated. Therefore, in this low fluid velocity range (0 – 4.7 m.h^{-1}), the corrosion rate did not seem to depend on the fluid velocity.

With current analyses and assuming that the kinetics of the surface coverage is linear, it is possible to estimate the time by which the coverage value would reach 1, situation for which the system and probably the global corrosion mechanism and kinetics will change. Extrapolation of the experimental data used in Figure 12 lead to the t_{lim} values displayed in Table 3: this exposure duration would range between 14 000 h and 33 000 h at 300 °C, depending on the studied alloys and the reactor position in the loop.

However, the in-loop exposure durations were too short to conclude further. It is therefore not yet possible to extrapolate the corrosion rate over the long term. Nonetheless, based on the autoclave tests results, once the surface is fully covered by ilmenite crystallites, it can be foreseen that the global corrosion rate will become very low. Consequently, the first key issue for the prevision of the corrosion of titanium alloys in PWR primary water seems to be the estimation of the corrosion rate before reaching the full coverage of the surface by ilmenite, which the present study partly addressed. The second key issue would be to investigate further the stability of this apparently protective layer.

5 Conclusions

- In pressurised water at 300 °C, uniform corrosion of titanium alloys samples was due to the simultaneous dissolution and growth of the continuous oxide layer, which is consistent with a Loriers-Haycock type model. This layer was made of rutile on CP Ti and of anatase on Ti64 and Ti10-2-3. The corrosion of the stainless steel reactors also released iron ions into the water. A part of the titanium hydroxides released by the corrosion of the sample precipitated into crystallites of ilmenite $FeTiO_3$ and anatase TiO_2, which participated in the mass uptake. The part that did not precipitate on the surface of the sample caused a mass loss due to the titanium dissolution.

- The alloying elements did not seem to affect the corrosion mechanisms and kinetics, except for the nature (rutile or anatase) of the continuous oxide layer grown at 300 °C.

- The corrosion rate appeared to be constant with the exposure duration until it dropped as the ilmenite coverage ratio reached 1. The mass uptake was consistent with this evolution. It was linear for very short durations and then became increasingly parabolic due to the increase in the fraction of ilmenite in the precipitated crystallites as exposure progressed. It would eventually stabilise as soon as the coverage ratio of ilmenite crystallites reached 1. In order to slow down corrosion, placing titanium components in a stainless steel circuit (which

is therefore in greater proportion) is a good combination provided the experimental conditions promote the formation of ilmenite.

- A method for estimating the corrosion rate was developed based on global measurements of mass variations and GD-OES analysis. It took into account the evolution of both the precipitation and the continuous oxide layer. The corrosion rate was estimated, for the three materials, between 2 and 6.6 µm.year^{-1} at 300 °C, with a precipitation ratio between 1 and 0.7 respectively in reactor 2 and a precipitation ratio between approximately 0.8 and 0.6 in reactor 1.

Acknowledgements

This work is the result of contributions that the authors would like to thank. The first thanks go to CEA, which made the study possible by funding it. The assistance of Frederic Datcharry from CEA was essential in the realisation of the high temperature and pressure exposures. The authors wish to thank Benoist Muzeau from CEA for the access and training in Raman spectroscopy. This research has benefited from characterisation equipment of the Grenoble INP - CMTC platform supported by the Centre of Excellence of Multifunctional Architectured Materials "CEMAM" n°ANR-10-LABX-44-01 funded by the Investments for the Future programme. Final thanks go to Stéphane Coindeau and Thierry Encinas from CMTC, for the DRX measurements and their processing, which were central to the material characterisations carried out.

Data availability

The raw/processed data required to reproduce these findings cannot be shared at this time due to technical or time limitations.

References

[1] M. Zucchetti, D. Boerman, and G. Piatti, « Characterisation of a titanium alloy for nuclear fusion applications », p. 17.

[2] Q. Bignon, F. Martin, Q. Auzoux, F. Miserque, M. Tabarant, L. Latu-Romain, Y. Wouters, « Oxide formation on titanium alloys in primary water of nuclear pressurised water reactor », *Corros. Sci.*, vol. 150, p. 32-41, avr. 2019, doi: 10.1016/j.corsci.2019.01.020.

[3] L. Zhang, D. Sun, and R. Xiong, « Study of corrosion kinetics and microstructure of α-phase pure titanium tube in environment 300°C and 8.6MPa water », *Corros. Sci.*, vol. 162, p. 108217, janv. 2020, doi: 10.1016/j.corsci.2019.108217.

[4] J. Kaneda, S. Kasahara, J. Kuniya, K. Moriya, F. Kano, N. Saito, A. Shioiri, T. Shibayama, H. Takahashi, « General corrosion properties of titanium based alloys for the fuel claddings in the supercritical water-cooled reactor », *Proc. 12th Int. Conf. Environ. Degrad. Mater. Nucl. Power Syst. React. Miner. Met. Mater. Soc.*, p. 1409-1418, 2005.

[5] E. Hillner, « Corrosion of Zirconium-Base Alloys—An Overview », *Zircon. Nucl. Ind.*, p. 211-235, janv. 1977, doi: 10.1520/STP35573S.

[6] R. Verlet, M. Tupin, G. Baldacchino, K. Wolski, S. Miro, D. Gosset, K. Colas, M. Jublot, F. Jomard, « Influence of light ion irradiation of the oxide layer on the oxidation rate of Zircaloy-4 », *Corros. Sci.*, vol. 98, p. 327-338, sept. 2015, doi: 10.1016/j.corsci.2015.05.045.

[7] J. Thomazet, A. Dalmais, P. Bossis, J. Godlewski, M. Blat, and A. Miquet, « The corrosion of the alloy M5: an overview », in *IAEA Technical Committee Meeting on Behavior of High Corrosion Resistance Zr-based Alloys*, 2005, p. 24-28.

[8] D. D. Macdonald, « The history of the Point Defect Model for the passive state: A brief review of film growth aspects », *Electrochimica Acta*, vol. 56, nº 4, p. 1761-1772, janv. 2011, doi: 10.1016/j.electacta.2010.11.005.

[9] I. Sekine, H. Sato, Y. Imatamari, N. Mukaida, M. Yuasa, L. Silao, S. Ono, M. Haginuma, « Corrosion Behavior of SUS 304 Stainless Steel in High Temperature and High Pressure Water Adding Metal Ions », *Zair.--Kankyo*, vol. 47, nº 4, p. 275-279, 1998, doi: 10.3323/jcorr1991.47.275.

[10] A. Machet, « Study of the initial satges of oxidation of stainless steels in high temperature water », Theses, Chimie ParisTech, 2004.

[11] S.-W. Kim, D.-J. Kim, and H.-P. Kim, « Evaluation of galvanic corrosion behaviour of SA-508 low alloy steel and type 309 L stainless steel cladding of reactor pressure vessel under simulated primary water environment », *Nucl. Eng. Technol.*, vol. 44, nº 7, p. 773-780, 2012, doi: 10.5516/NET.07.2011.054.

[12] Q. Bignon, « Oxydation et prise d'hydrogène d'alliages de titane en milieu primaire de réacteur à eau pressurisée: mécanismes, cinétiques et effet sur le comportement mécanique », Thèse, Grenoble Alpes, 2018.

[13] A. V. Bandura and S. N. Lvov, « The Ionization Constant of Water over Wide Ranges of Temperature and Density », *J. Phys. Chem. Ref. Data*, vol. 35, nº 1, p. 15-30, mars 2006, doi: 10.1063/1.1928231.

[14] P. Hurst, D. A. Appleton, P. Banks and A. S. Raffel, « Slow strain rate stress corrosion tests on A508-III and A533B steel in de-ionized and PWR water at 56K », *Corros. Sci.*, vol. 25, nº 8, p. 651-671, janv. 1985, doi: 10.1016/0010-938X(85)90004-6.

[15] S.-H. Jeon, H.-S. Shim, J.-M. Lee, J. Han and D. H. Hur, « Simulation of Porous Magnetite Deposits on Steam Generator Tubes in Circulating Water at 270 °C », *Crystals*, vol. 10, nº 9, Art. nº 9, sept. 2020, doi: 10.3390/cryst10090729.

[16] M. Sennour, L. Marchetti, F. Martin, S. Perrin, R. Molins and M. Pijolat, « A detailed TEM and SEM study of Ni-base alloys oxide scales formed in primary conditions of pressurized water reactor », *J. Nucl. Mater.*, vol. 402, nº 2, p. 147-156, juill. 2010, doi: 10.1016/j.jnucmat.2010.05.010.

[17] E. F. Rauch and M. Véron, « Automated crystal orientation and phase mapping in TEM », *Mater. Charact.*, vol. 98, p. 1-9, déc. 2014, doi: 10.1016/j.matchar.2014.08.010.

[18] S. Hashimoto, A. Tanaka, A. Murata, and T. Sakurada, « Formulation for XPS spectral change of oxides by ion bombardment as a function of sputtering time », *Surf. Sci.*, vol. 556, nº 1, p. 22-32, mai 2004, doi: 10.1016/j.susc.2004.03.002.

[19] K. G. Knauss, M. J. Dibley, W. L. Bourcier, and H. F. Shaw, « Ti(IV) hydrolysis constants derived from rutile solubility measurements made from 100 to 300°C », *Appl. Geochem.*, vol. 16, nº 9-10, p. 1115-1128, juill. 2001, doi: 10.1016/S0883-2927(00)00081-0.

[20] W. G. Cook and R. P. Olive, « Pourbaix diagrams for chromium, aluminum and titanium extended to high-subcritical and low-supercritical conditions », *Corros. Sci.*, vol. 58, p. 291-298, mai 2012, doi: 10.1016/j.corsci.2012.02.002.

[21] E. W. Haycock, « Transitions from Parabolic to Linear Kinetics in Scaling of Metals », *J. Electrochem. Soc.*, vol. 106, nº 9, p. 771-775, janv. 1959, doi: 10.1149/1.2427495.

[22] J. Loriers, « Loi d'oxydation du cérium métallique. Généralisation à d'autres métaux. », *Académie Sci.*, vol. 231, p. 522-524, sept. 1950.

Figure captions:

Figure 1: Schematical representation of the corrosion loop used for the exposure of CP Ti, Ti64 and Ti10-2-3 samples located in reactor 2 (downstream) for short exposure durations and in reactor 1 (upstream) for long exposure durations (3499 h). The arrows indicate the primary water circulation direction.

Figure 2: XRD diffractograms (grazing incidence 1.5 °) on CP Ti exposed for 3499 h in primary water at 300 °C.

Figure 3: SEM (secondary electrons) observations of cross sections of CP Ti samples after a) 217 h, b) 834 h, c and d) 3499 h of exposure at 300 °C. d) Magnification of a local attack site showing the continuous oxide layer.

Figure 4: Observations of the zones of interest on a cross-sectional TEM slide of the CP Ti exposed 3499 h at 300 °C. a) shows a bright field STEM image of areas of interest, showing the spongy zone in yellow. b) TEM-ASTAR phase map combined with index showing Ti metal and rutile oxide phase. c) TEM-ASTAR orientation map combined with index. For colours, the reader is asked to refer to the online version of the paper.

Figure 5: Bright-Field STEM image-EDS maps of Ti – in yellow – and O – in red – (K_α rays) with intensity profiles in overlay integrated on the zone underlined by a blue rectangle in a CP Ti sample exposed 3499 h to primary water at 300 °C in reactor 2. The red arrow shows the protective deposit in W of the TEM foil. The oxide is indexed with the yellow arrow on the Ti substrate. For colours, the reader is asked to refer to the online version of the paper.

Figure 6: SEM (SE) observations of cross sections of CP Ti, Ti64, and Ti10-2-3 after exposure for 7560 h at 300 °C to primary water in the autoclave showing a full coverage of the surface by $FeTiO_3$ ilmenite large crystallites. The thin continuous TiO_2 layer is indicated by the black arrows.

Figure 7: Evolution of the mean continuous oxide layer thickness of CP Ti, Ti64 and Ti10-2-3 with exposure duration at 300 °C in reactor 1 (R1) and reactor 2 (R2), measured from SEM - SE observations (20 images treated per data point). The native continuous oxide thickness was determined by XPS.

Figure 8: Illustration of the method used to estimate the mean corroded metal depth, here for CP Ti exposed 3499 h at 300 °C in primary water. The black line represents the reference line, assumed as the initial position of the sample's surface. The red hatched areas represent the corroded metal areas.

Figure 9: Evolution of the mean corroded metal depth as a function of the exposure duration for the three materials exposed in reactor 1 (R1) and reactor 2 (R2) at 300 °C.

Figure 10: GD-OES concentration profile (at.%) obtained on Ti10-2-3 after 834 hours exposure at 300 °C in primary media showing the Fe profile and the area used for integration (grey) to estimate n_{Fe} and the O profile and the area used for integration (red) to estimate n_O.

Figure 11: Approximately linear evolution of the ratio $q = \frac{n_{FeTiO_3}}{n_{FeTiO_3} + n_{TiO_2}}$ *with the exposure duration for the three materials in reactor 1 (R1) and reactor 2 (R2) at 300 °C. The slopes of the linear fit for each material are given in Table 1.*

Figure 12: Evolution of the mean coverage ratio of ilmenite $FeTiO_3$ as a function of the exposure duration of CP Ti, Ti64 and Ti10-2-3 in reactor 1 (R1) and reactor 2 (R2) at 300 °C measured from 10 optical microscope observations for each duration and material.

Tables:

Tables

300 °C	CP Ti	Ti64	Ti10-2-3
α (h^{-1})	1.1 x 10^{-4}	3.7 x 10^{-5}	9.6 x 10^{-5}

Table 1: Slopes of the linear fits obtained from the q ratio measurements (in Figure 11) after each exposure duration at 300 °C for all the three materials.

Titanium precipitation ratio *p*(R2) Reactor 2 (enriched medium)	Estimated corrosion rate *r* (µm.$year^{-1}$)	Titanium precipitation ratio *p*(R1) Reactor 1 (purified medium)
0.7	6.6	0.58 ± 0.04
0.8	3.6	0.65 ± 0.04
0.9	2.8	0.70 ± 0.04
1	2	0.79 ± 0.04

Table 2: Sets of {p(R2), r, p(R1)} triplets adjusted for CP Ti, Ti64 and Ti10-2-3 after exposure at 300 °C to pressurised water by varying p(R2).

	Exposure duration at 300 °C t_{lim} (10^3 h)	
Reactor	R1	R2
CP Ti	26	19
Ti64	29	33
Ti10-2-3	14	14

Table 3: Estimation of the necessary exposure duration t_{lim} to reach an ilmenite coverage ratio of 1 from the extrapolation of the linear fits in Figure 12 depending on materials and reactor position in the corrosion loop.

Figures

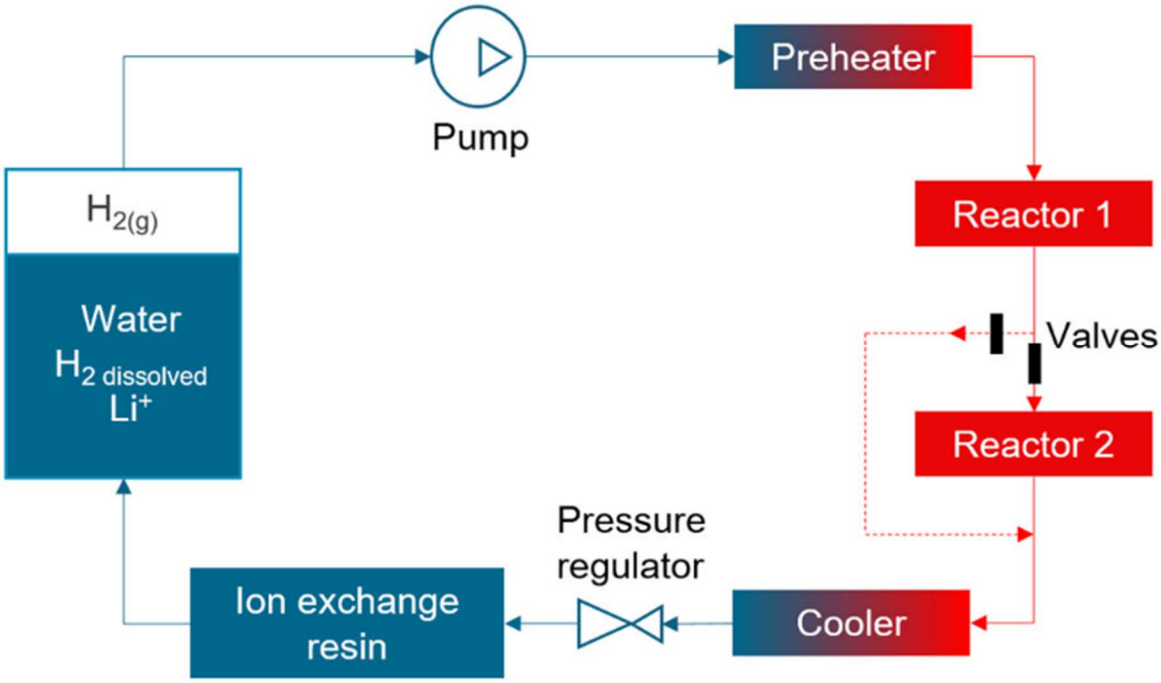

Figure 1

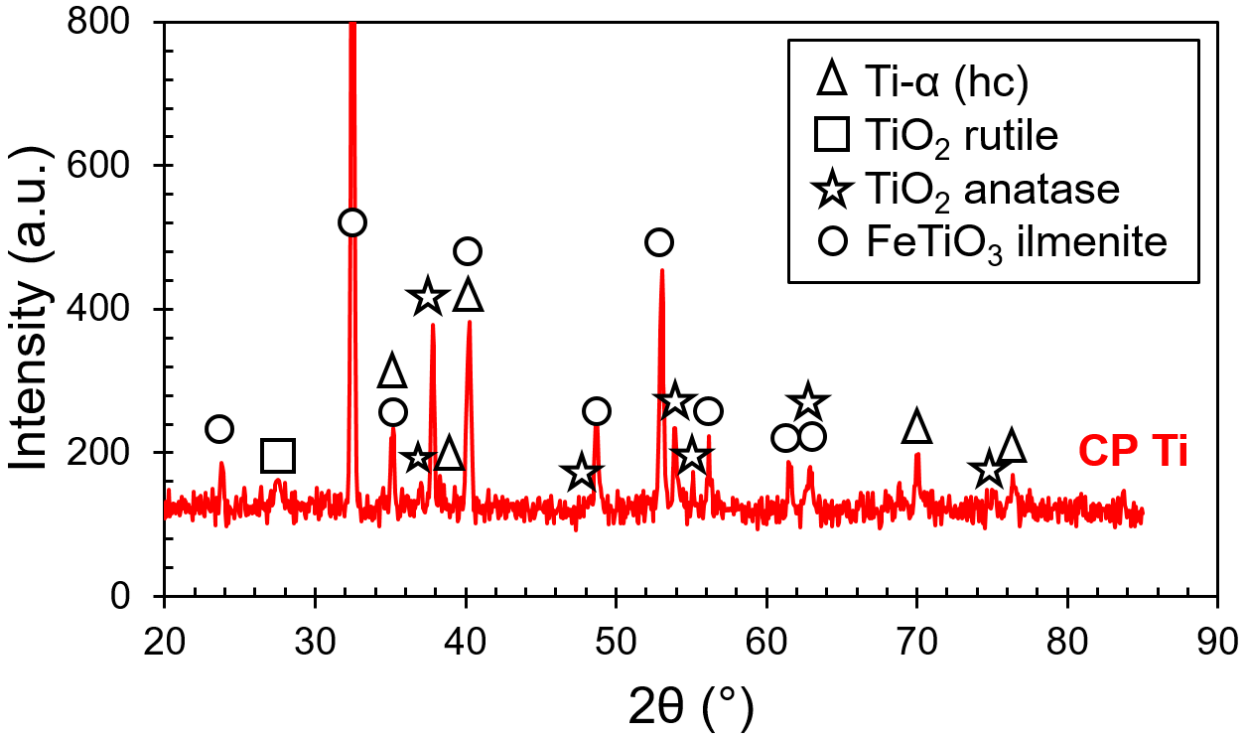
Intensity (a.u.)
2θ (°)
Ti-α (hc)
TiO2 rutile
TiO2 anatase
FeTiO3 ilmenite
CP Ti

Figure 2

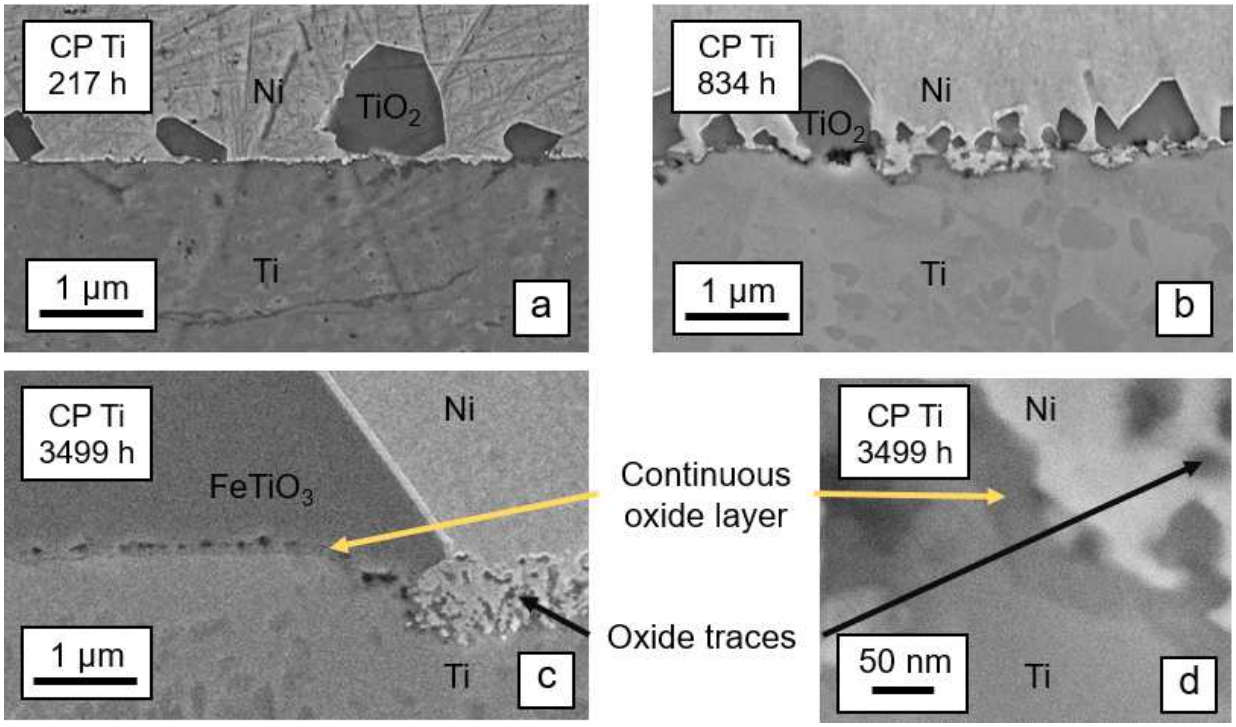
CP Ti
217 h
Ni
TiO_2
Ti
1 µm
a
CP Ti
834 h
Ni
TiO_2
Ti
1 µm
b
CP Ti
3499 h
Ni
$FeTiO_3$
Ti
1 µm
c
Continuous
oxide layer
Oxide traces
CP Ti
3499 h
Ni
Ti
50 nm
d

Figure 3

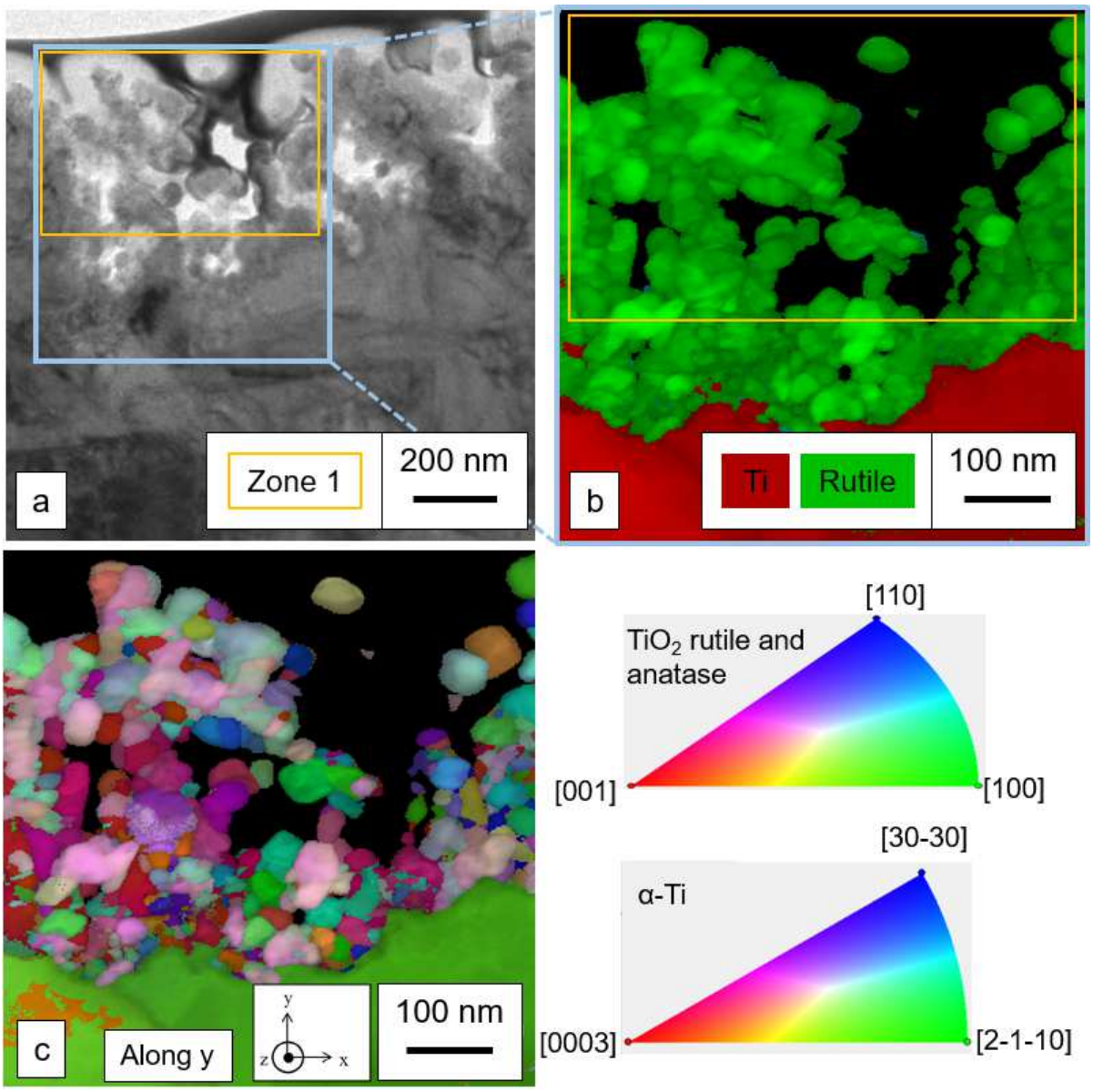
a
Zone 1
200 nm
b
Ti
Rutile
100 nm
c
Along y
y
z
x
100 nm
[110]
TiO2 rutile and anatase
[001]
[100]
[30-30]
α-Ti
[0003]
[2-1-10]

Figure 4

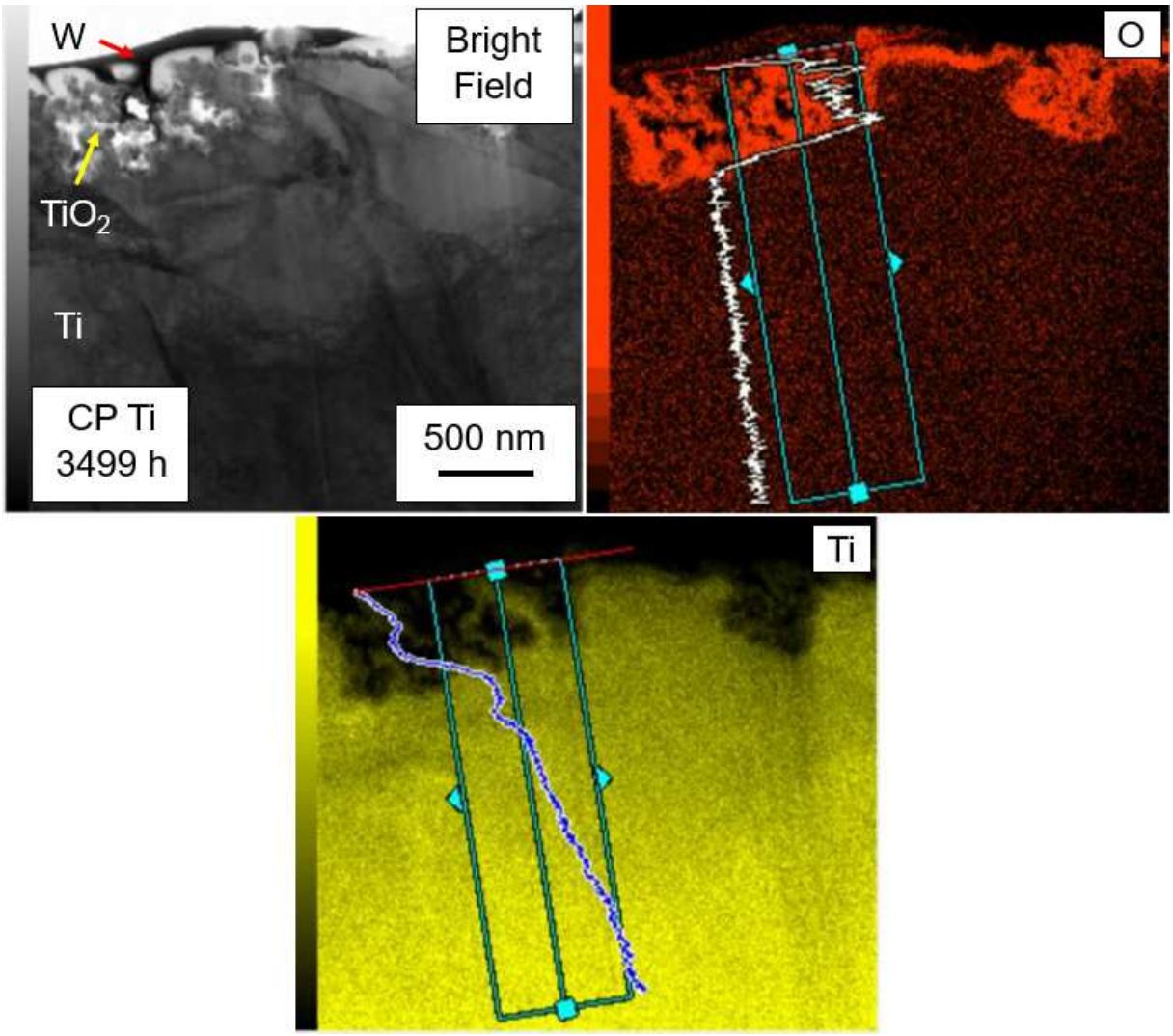

Figure 5

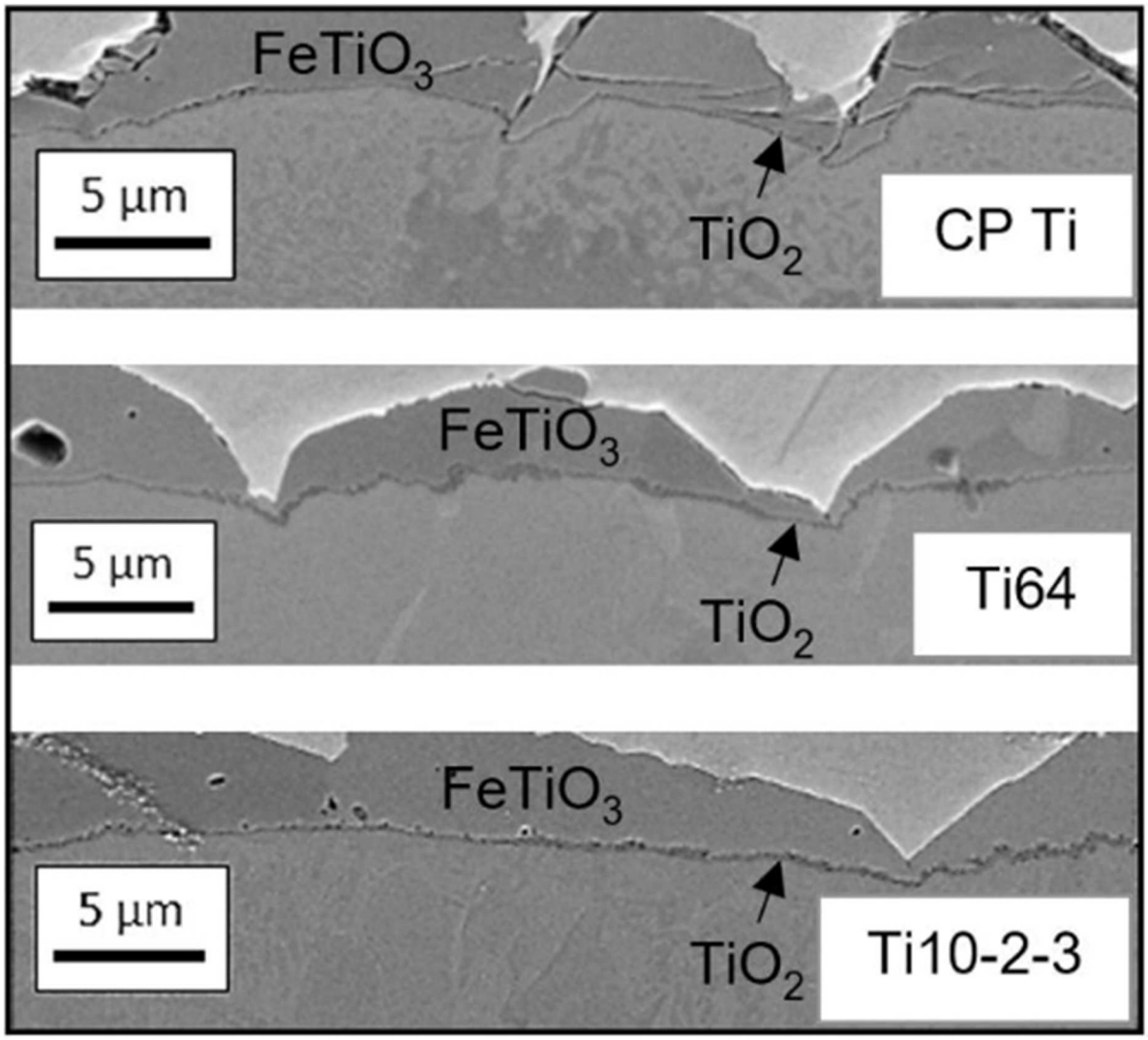
FeTiO3
5 µm
TiO2
CP Ti
FeTiO3
5 µm
TiO2
Ti64
FeTiO3
5 µm
TiO2
Ti10-2-3

Figure 6

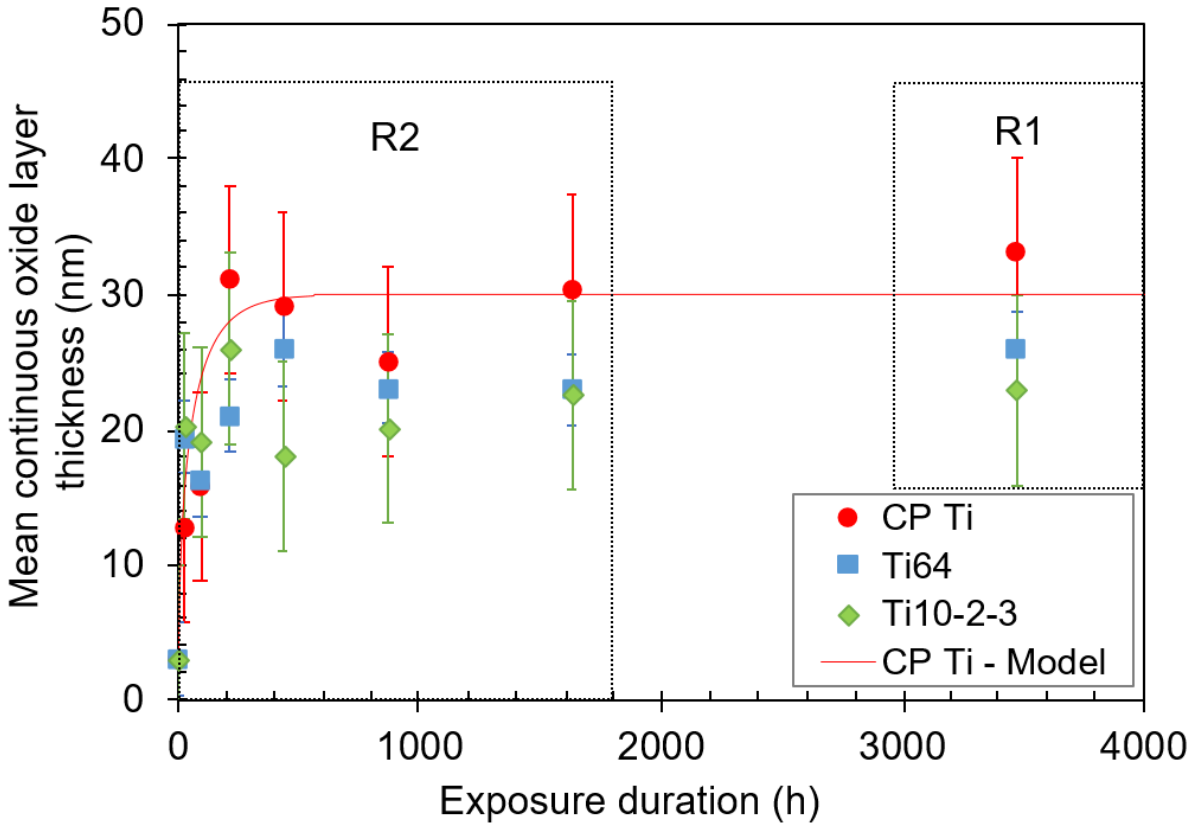
Mean continuous oxide layer thickness (nm)
Exposure duration (h)
R2
R1
CP Ti
Ti64
Ti10-2-3
CP Ti - Model
0
10
20
30
40
50
0
1000
2000
3000
4000

Figure 7

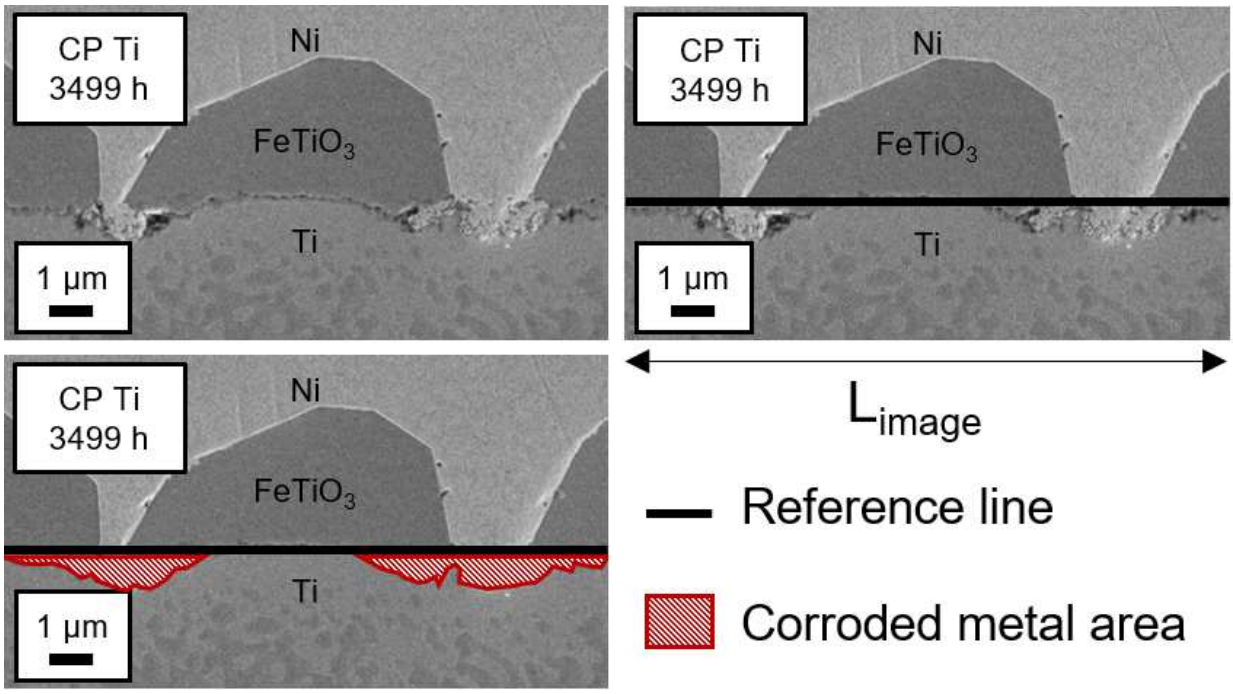
CP Ti
3499 h
Ni
FeTiO3
Ti
1 µm
CP Ti
3499 h
Ni
FeTiO3
Ti
1 µm
CP Ti
3499 h
Ni
FeTiO3
Ti
1 µm
Limage
Reference line
Corroded metal area

Figure 8

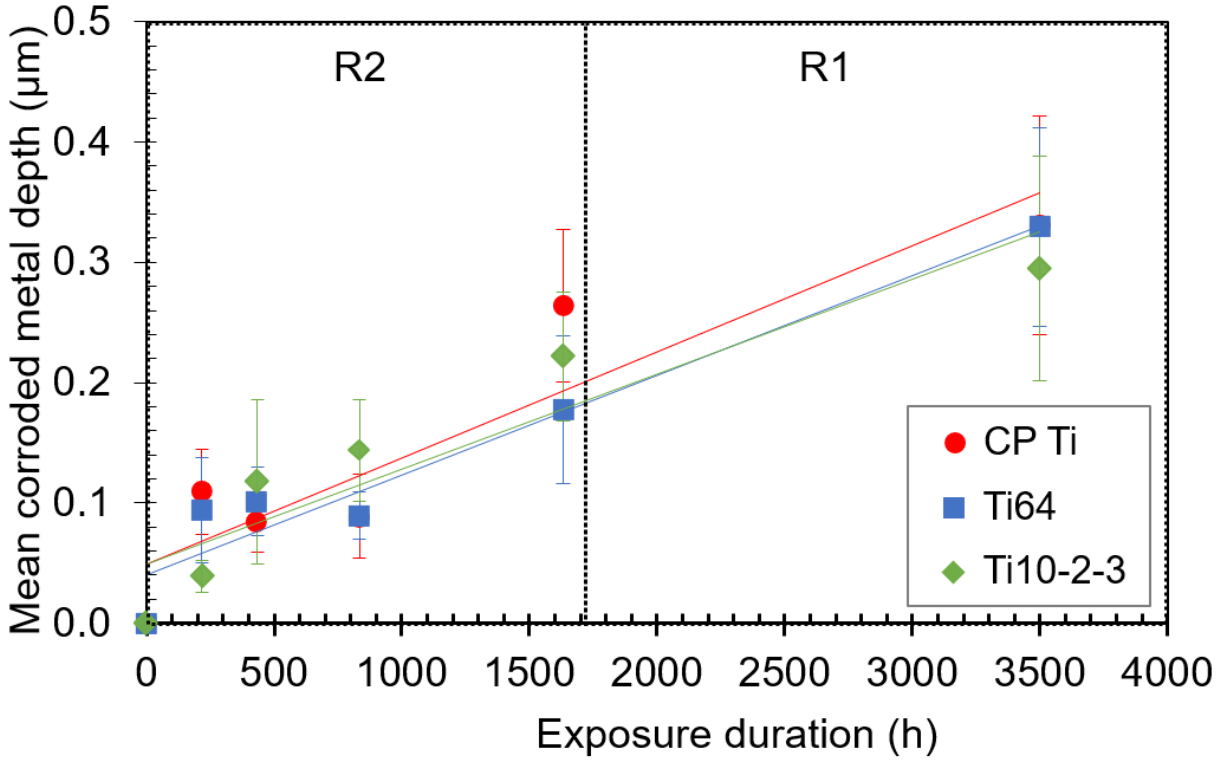
R2
R1
Mean corroded metal depth (µm)
0.0
0.1
0.2
0.3
0.4
0.5
0
500
1000
1500
2000
2500
3000
3500
4000
Exposure duration (h)
CP Ti
Ti64
Ti10-2-3

Figure 9

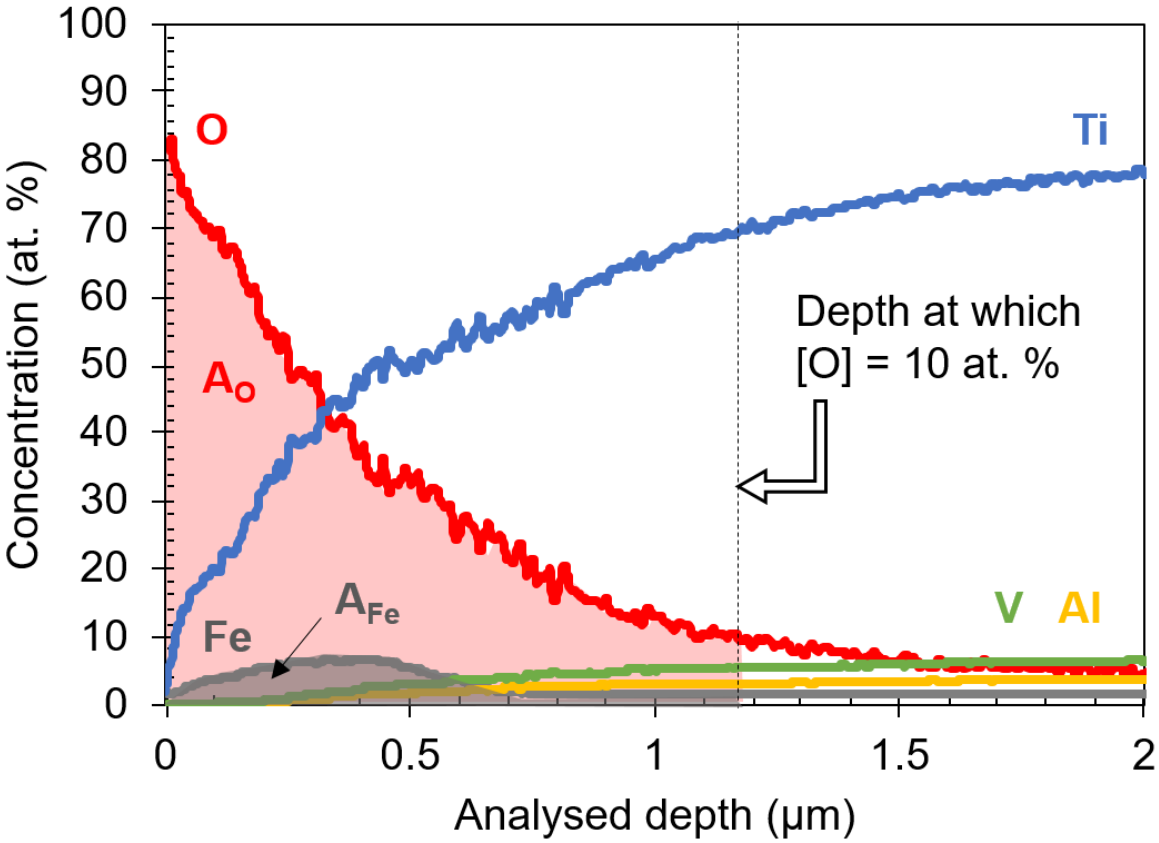
100
90
80
70
60
50
40
30
20
10
0
Concentration (at. %)
0
0.5
1
1.5
2
Analysed depth (µm)
O
Ti
Depth at which
[O] = 10 at. %
A_O
A_Fe
Fe
V
Al

Figure 10

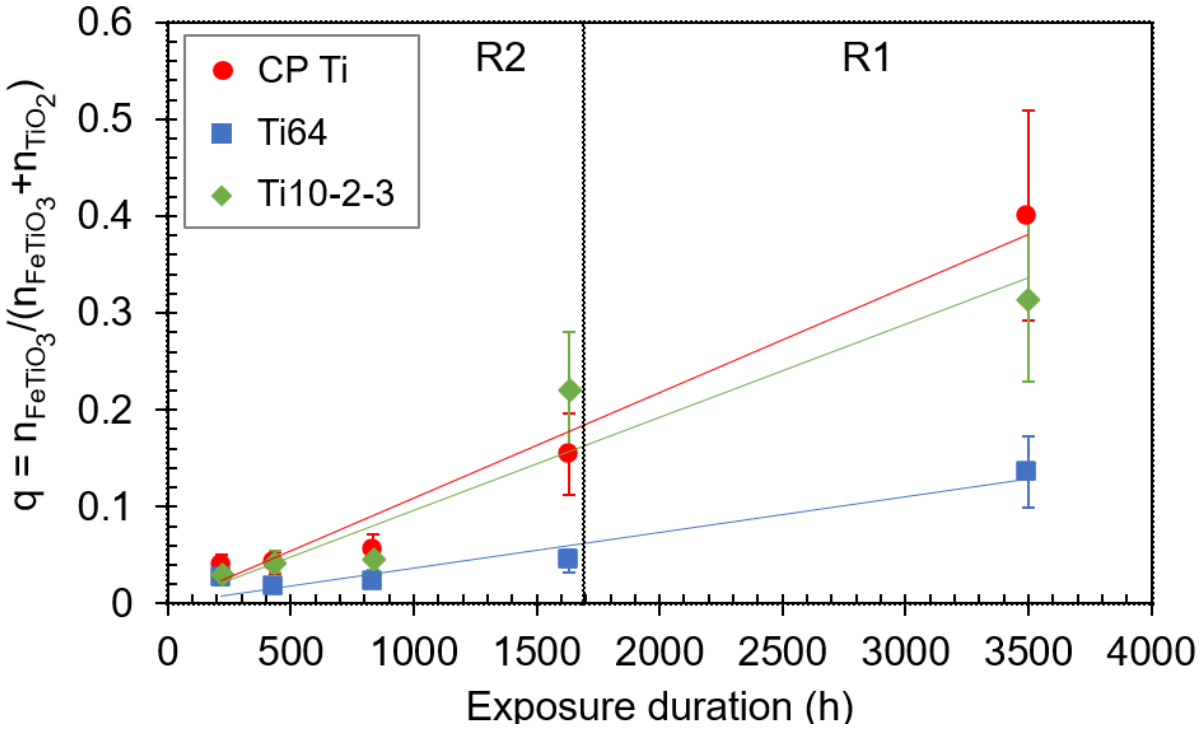
CP Ti
Ti64
Ti10-2-3
R2
R1
$q = n_{FeTiO_3}/(n_{FeTiO_3}+n_{TiO_2})$
Exposure duration (h)
0
0.1
0.2
0.3
0.4
0.5
0.6
0
500
1000
1500
2000
2500
3000
3500
4000

Figure 11

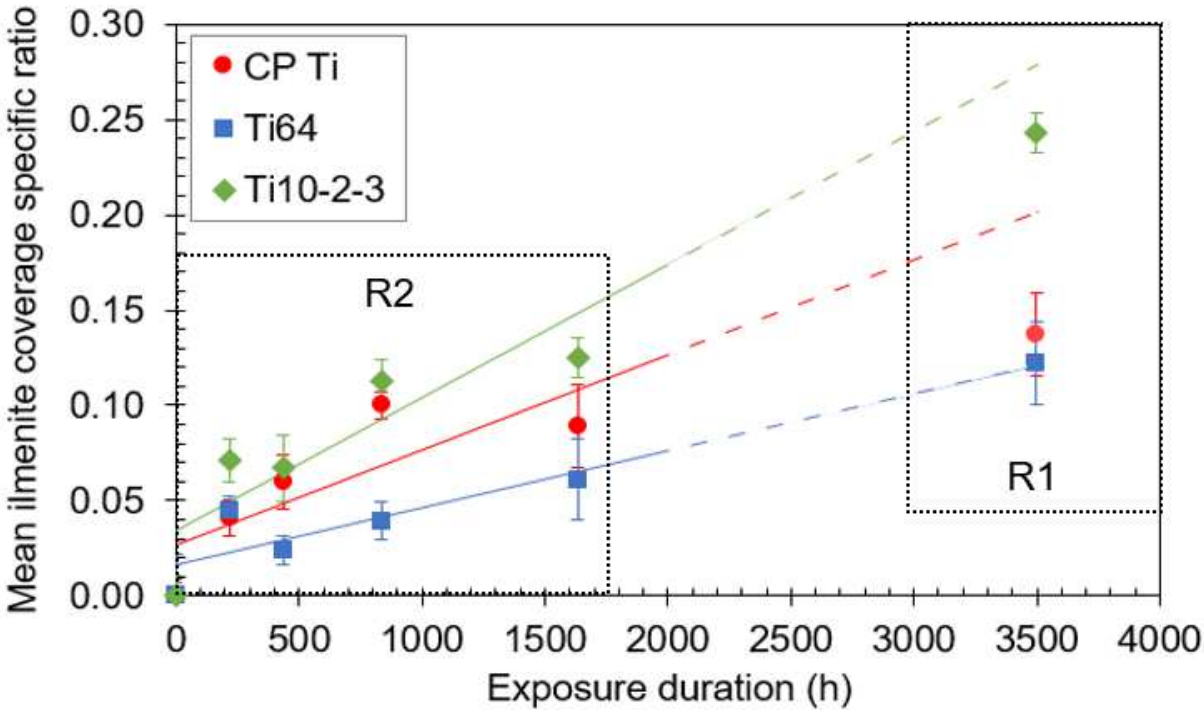
Mean ilmenite coverage specific ratio
0.30
0.25
0.20
0.15
0.10
0.05
0.00
CP Ti
Ti64
Ti10-2-3
R2
R1
0
500
1000
1500
2000
2500
3000
3500
4000
Exposure duration (h)

Figure 12

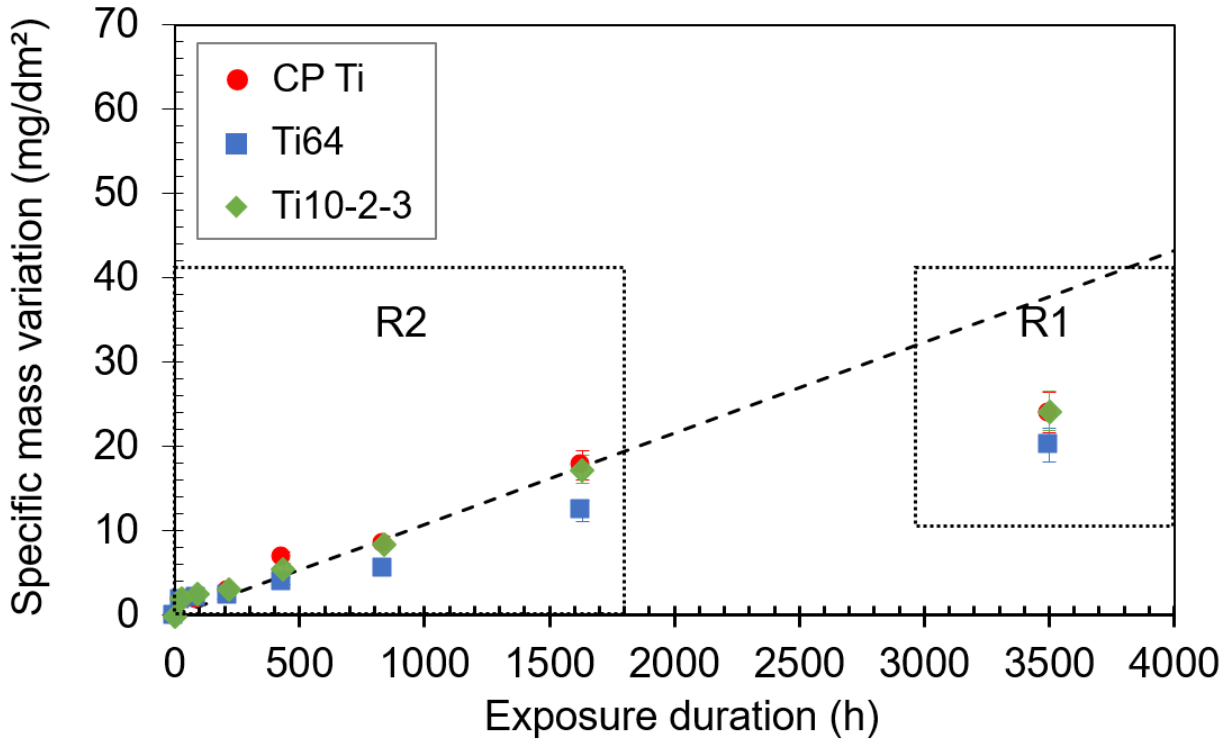
Specific mass variation (mg/dm²)
70
60
50
40
30
20
10
0
CP Ti
Ti64
Ti10-2-3
R2
R1
0
500
1000
1500
2000
2500
3000
3500
4000
Exposure duration (h)

Figure 13

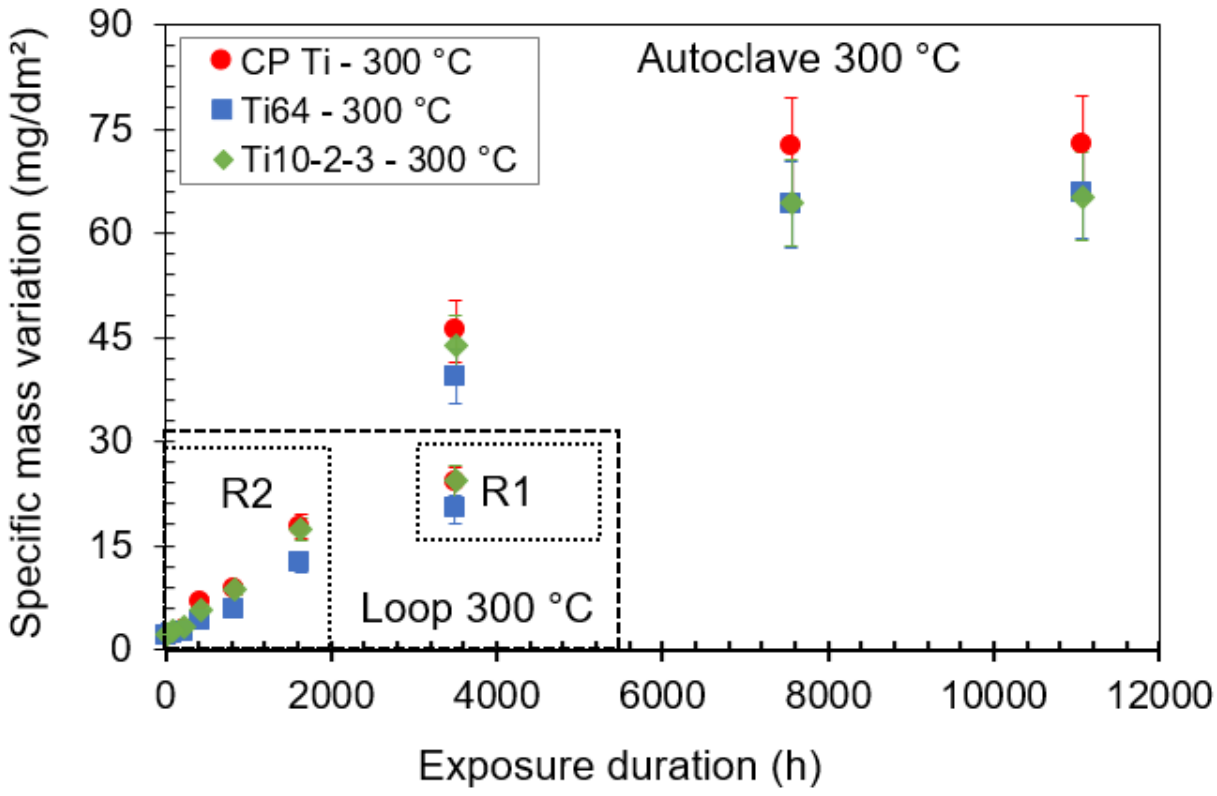
CP Ti - 300 °C
Ti64 - 300 °C
Ti10-2-3 - 300 °C
Autoclave 300 °C
R2
R1
Loop 300 °C
Specific mass variation (mg/dm²)
Exposure duration (h)
0
15
30
45
60
75
90
0
2000
4000
6000
8000
10000
12000

Figure 14

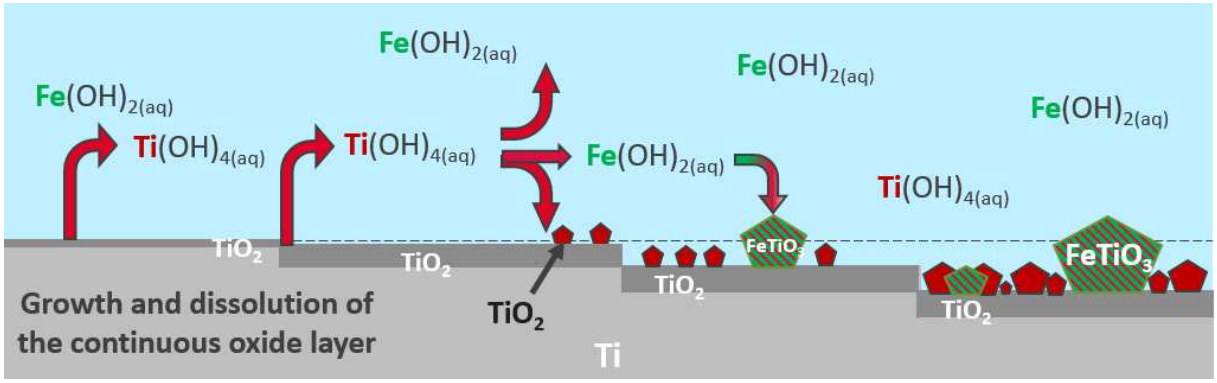
Fe(OH)2(aq)
Ti(OH)4(aq)
Fe(OH)2(aq)
Ti(OH)4(aq)
Fe(OH)2(aq)
Fe(OH)2(aq)
Ti(OH)4(aq)
Fe(OH)2(aq)
TiO2
TiO2
TiO2
FeTiO3
TiO2
FeTiO3
TiO2
Growth and dissolution of
the continuous oxide layer
Ti

Figure 15

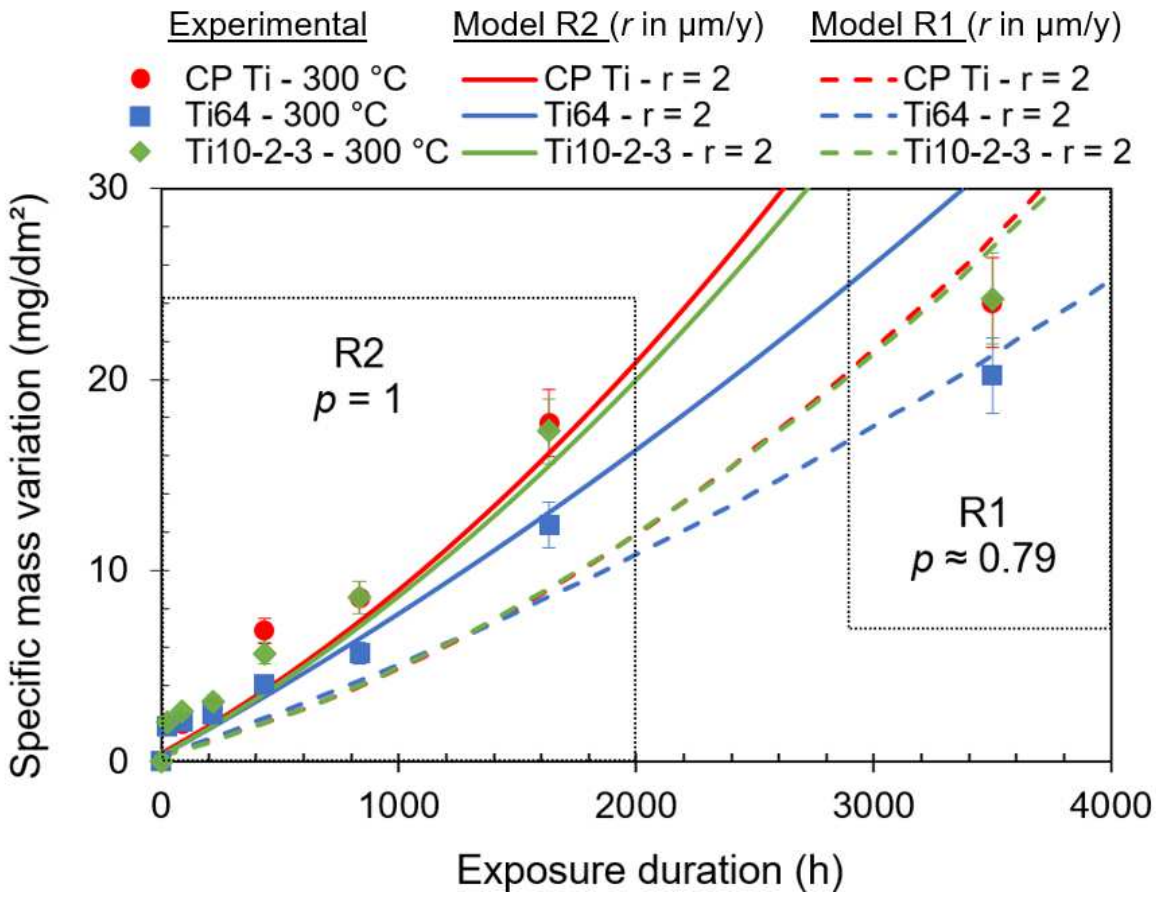
Experimental
Model R2 (r in µm/y)
Model R1 (r in µm/y)
CP Ti - 300 °C
Ti64 - 300 °C
Ti10-2-3 - 300 °C
CP Ti - r = 2
Ti64 - r = 2
Ti10-2-3 - r = 2
CP Ti - r = 2
Ti64 - r = 2
Ti10-2-3 - r = 2
R2
p = 1
R1
p ≈ 0.79
Specific mass variation (mg/dm²)
Exposure duration (h)
0
10
20
30
0
1000
2000
3000
4000

Figure 16